Electron affinity and binding energy of excitons in disordered organic semiconductors. II. First-principles simulations and inverse photoemission studies for MADN

Gianluca Tirimbò [1,2] O. Nagaoka [3,4] S. Fukushima [3,4] Clint van Hoesel [5] Hiroyuki Yoshida [3,4]
Reinder Coehoorn [2,5] and Björn Baumeier [1,2,*]

[1]*Department of Mathematics and Computer Science, Eindhoven University of Technology, P.O. Box 513, 5600MB Eindhoven, The Netherlands*
[2]*Institute for Complex Molecular Systems, Eindhoven University of Technology, P.O. Box 513, 5600MB Eindhoven, The Netherlands*
[3]*Graduate School of Engineering, Chiba University, 1-33 Yayoi-cho, Inage-ku, Chiba 263-8522, Japan*
[4]*Molecular Chirality Research Center, Chiba University, 1-33 Yayoi-cho, Inage-ku, Chiba 263-8522, Japan*
[5]*Department of Applied Physics and Science Education, Eindhoven University of Technology, P.O. Box 513, 5600MB Eindhoven, The Netherlands*

(Received 21 July 2025; revised 17 September 2025; accepted 5 November 2025; published 4 December 2025)

Key quantities for designing new opto-electronic devices that are based on disordered organic semiconductors, such as organic light-emitting diodes (OLEDs), are the frontier orbital energies, exciton energies, and exciton binding energies. Obtaining these quantities spectroscopically with a high accuracy is complicated by the nonadiabaticity of such experiments. Here, we present, for two isomers of the blue-emitting prototypical OLED material 2-methyl-9,10-bis(naphthalen-2-yl)anthracene (MADN), multiscale first-principles simulations of optical absorption spectra and of the electron affinity E_A, a theoretical prediction and analysis of low-energy inverse photoemission spectroscopy (LEIPS) spectra that probe E_A, and experimental LEIPS spectra. The simulations combine many-body Green's function theory, polarizable film embedding, and multimode electron-vibrational coupling. We show how the onset energy of LEIPS spectra, which is commonly used to estimate E_A, can differ from the actual adiabatic value, depending on material parameters and the instrumental resolution. For the two isomers of MADN, the theoretical and experimental onset energies differ by about 0.20–0.25 eV, which is within the expected uncertainty margin. However, the experimental spectra are almost featureless, whereas the theoretical spectra show a clear peak structure. An extensive study is presented of the possible effects of thin-film charging on the spectra, including charging of deep trap states. The calculated optical absorption spectra agree excellently with experiment, with a peak energy difference of only about 0.05 eV. For the two isomers of MADN, the calculated adiabatic singlet exciton binding energies are 1.0–1.1 eV.

DOI: 10.1103/6gh2-8lb8

I. INTRODUCTION

Organic semiconductors offer a wide range of applications in novel electronic or optoelectronic devices, such as organic light-emitting diodes (OLEDs) or organic solar cells (OPVs). Developing a detailed understanding and optimization of the observed phenomena and the device operation requires knowledge of the fundamental electronic properties of the systems [1]. For instance, the nature of the frontier orbitals, the ionization energy and electron affinity, and the nature of the excited electronic states are of great importance to processes such as light absorption and emission, photoconductivity, and electroluminescence [2]. Predictive multiscale modeling of OLEDs, for example with the purpose of accelerating the development of higher-efficiency displays with an extended operational lifetime, requires that accurate experimentally validated energy levels and process rates are available [3–6].

The ionization energy E_{IE} can be obtained from ultraviolet photoelectron spectroscopy (UPS). In a recent study, we have shown that a first-principles-based multiscale simulation approach can provide an accurate prediction of UPS spectra [7]. The study was carried out for thin structurally disordered (amorphous) films of the α and β isomers of the prototypical ambipolar and blue host material 2-methyl-9,10-bis(naphthalen-2-yl)anthracene (MADN) [8–12], and also showed that various corrections to the conventionally used spectral onset energy are needed to obtain the ionization energy. The simulated UPS spectrum agreed excellently with experiment. Measuring the electron affinity E_{EA} and the singlet exciton binding energy $E_{S,b}$ is more difficult. The unoccupied energy-level structure can be studied experimentally by low-energy inverse-photoemission spectroscopy (LEIPS) [13,14]. The technique has recently been used to study the electron affinity in various organic semiconductors [15–19]. However, a methodology for obtaining, from the spectra, accurate values of the electron affinity has not yet been developed. One may expect that corrections that are analogous

*Contact author: b.baumeier@tue.nl

Published by the American Physical Society under the terms of the Creative Commons Attribution 4.0 International license. Further distribution of this work must maintain attribution to the author(s) and the published article's title, journal citation, and DOI.

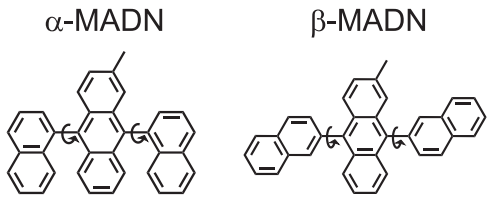


FIG. 1. Molecular structures of α-MADN and β-MADN. The naphthyl side groups are rotated out of the plane of the anthracene core to 90° dihedral angles, as indicated with arrows.

to those that are needed to obtain E_{IE} from UPS spectra will also be required to obtain E_{EA} from LEIPS spectra. Similar corrections to the spectral onset energy that is conventionally used to estimate the electron affinity from LEIPS spectra could also affect the values of the polarization energies (see, e.g., Ref. [18]) and the exciton binding energies [20] that are obtained using LEIPS experiments. Alternative methods for measuring the singlet exciton binding energy are not well established. In paper I of this series of three papers [21], a simulation-assisted method for obtaining $E_{\mathrm{S,b}}$ from field-induced dissociation (FID) experiments was proposed. However, this methodology has not yet been validated.

In this paper, we present a first-principles-based multiscale simulation approach from which the electron affinity, the optical absorption spectrum, and the exciton binding energy in disordered small-molecule organic semiconductors are derived. The simulation method consists of an accurate evaluation of (i) quasiparticle and exciton energy levels within the *GW* approximation with the Bethe-Salpeter equation (BSE), (ii) thin-film embedding effects, using a hybrid quantum-mechanics/molecular-mechanics (QM/MM) approach that takes the molecular polarizabilities and the long-range interactions due to partially ordered static multipole moments into account, and (iii) a full-quantum treatment of electron-vibration coupling. The theoretical methodology that is used is made possible by the large contrast between the strong intramolecular electronic and vibrational interactions of the *s-p* bonded atoms that comprise the organic molecules that are studied and the weak (van der Waals–type) intermolecular interactions. As a result, electronic, excitonic, and vibrational states are strongly localized on each of the molecules, and charge and exciton transfer to a neighbor molecule are relatively slow incoherent processes [2]. We show how the simulations can be used to obtain theoretical LEIPS spectra and how various material-specific and instrumental effects lead, in general, to a difference between the spectral onset energy and E_{A}. The approach is demonstrated for the α and β isomers of MADN (Fig. 1), for which experimental LEIPS spectra are also presented. While the UPS signal for both isomers showed a clear highest occupied molecular orbital (HOMO) peak, well-separated from the lower-energy parts (see Ref. [7]), the experimental LEIPS signal near the spectral onset and up to the vacuum energy is almost featureless. It is not immediately obvious whether the reason for the lack of features can be attributed to a small separation between lowest unoccupied molecular orbital (LUMO) and higher levels in MADN, strong vibrational broadening, surface effects, experimental conditions, or a combination of some of these factors. It is also unclear how one can relate this measured spectrum to the electron affinity of the material in the bulk. To remedy this situation and to remove these ambiguities in the determination of the electron affinity, we have refined our previous model [7] to account for several *GW* quasiparticle states (LUMO and higher). In addition, we study the possible spectral broadening due to thin-film charging.

The paper is organized as follows. In Sec. II, we provide an overview of the methodology and computational details of the electron affinity calculations. Section III shows, for thin films of α-MADN and β-MADN, the calculated layer-resolved density of electron states, in the bulk and near the surface, the calculated LEIPS spectra, and an analysis of the various effects that determine the difference between the spectral onset energy and the adiabatic value of the LUMO energy. Section IV shows the experimental LEIPS spectra and a comparison of these spectra with the simulation results. In Sec. V, we present the results of optical absorption simulations, a comparison with experimental spectra, the singlet exciton binding energies that follow from the simulations, and a quantification of the various energy-level correlations. A summary and outlook section (Sec. VI) concludes the paper. In paper III of this series [22], a more extensive experimental validation of the theoretical method is presented, using optical absorption, photoluminescence, and field-induced dissociation experiments.

Concerning the notation of theoretically calculated quantities, we remark that frontier orbital energies are indicated by the symbol ε, exciton energies are indicated by the symbol Ω, and energy differences (gap energies, binding energies, ionization energy, and electron affinity) are indicated by the symbol E, unless specified otherwise.

II. ELECTRON AFFINITY SIMULATIONS—THEORETICAL METHODOLOGY

In this section, we discuss the methods that have been used to calculate the distribution of the electron affinity in a thin film under the assumption that adding an electron to the ground state does not give rise to a change of the molecular structure (*vertical* quasiparticle energies). The stabilization due to molecular reorganization, which enhances the electron affinity, is discussed in Sec. III.

The approach is presented in detail in Ref. [23]. In summary, it is based on the assumption that (i) excitations inside the film remain localized on single molecules and (ii) electronic interactions of that excitation with the full molecular environment are purely electrostatic, i.e., quantum effects from exchange and/or correlation are negligible. The appropriateness of this approach follows from the weak (van der Waals) nature of the intermolecular interactions. As a result, intermolecular electron or hole transfer integrals are, for both isomers of MADN, only of the order of 1–10 meV [24], which is much smaller than the disorder energies (widths of the HOMO and LUMO energy distributions, ∼0.1 eV), the reorganization energies when creating a hole or an electron (∼0.1 eV), and the intramolecular (interatomic) transfer integrals (∼1 eV), so that the electron and hole states are strongly localized on each molecule. The small intermolecular charge transfer is, in part, due to the methyl and naphthyl side groups

of the MADN molecules. Their presence increases the average distance between the anthracene core parts of the molecule on which the frontier orbital electron and hole wave functions are located (see Fig. S1 of the Supplemental Material [25]). For the same reason, the excited states are also strongly localized. The coupling of the intramolecular vibrational modes ("vibrons") of different molecules, which can be significant in molecular crystals [26], is therefore strongly reduced. In this work, this coupling is neglected. The coupling of excitonic modes with vibrons (exciton-vibron coupling) is successfully described using a multimode extension of the Huang-Rhys formalism [2] that has been developed in Ref. [27], as will be shown in Fig. 9. The ionization energy, electron affinity and excitonic energies of small-molecule organic materials are, for these reasons, often obtained from quantum-chemical simulations for single molecules within which the thin-film embedding of the molecule is taken into account using a dielectric continuum solvation model, such as, e.g., COSMO [28]. However, in this work, we use a more advanced approach, within which the total system is split into a quantum (QM) region comprising a single molecule (sub-nm scale) and an embedding environment region (the rest of the film on the scale of 10–100 nm) whose interactions within itself and the QM region are modeled with a classical method (MM). Such a splitting makes the problem tractable, as a full QM treatment of a disordered molecular film consisting of 1000 molecules is impossible. At the same time, it contains not only the effects of intramolecular structural disorder in the geometries of the individual molecules on the excitation energies, but, more importantly, the effects on the distributions of the ionization energy, electron affinity, and singlet exciton energy of the intermolecular structural disorder and thin-film nature on the mesoscale (see below). All steps of the calculations take explicit atomic details into account.

A. Single-molecule quasiparticle energies in the *GW* approximation

The intramolecular contributions to the embedded excitation energies of individual molecules are determined as effective single-particle energies including quasiparticle corrections within the *GW* approximation of many-body Green's function theory [29,30]. In the following, a brief overview of the basic ingredients to this method is given. For a full account, consider, e.g., Refs. [23,31] and [32]. We use atomic (Hartree) units [$\hbar = 1$, $m_e = 1$ and $e^2/(4\pi\varepsilon_0) = 1$, with m_e the electron mass, e the elementary electron charge, and ε_0 the vacuum permittivity].

The quasiparticle corrections are based on and applied to solutions of the Kohn-Sham (KS) density functional theory (DFT) equations [33],

$$[T_0 + V_{\text{ext}} + V_{\text{Hartree}} + V_{\text{xc}}]\left|\phi_i^{\text{KS}}\right\rangle = \varepsilon_i^{\text{KS}}\left|\phi_i^{\text{KS}}\right\rangle. \quad (1)$$

Here, T_0 is the kinetic-energy operator, V_{ext} is the external potential, V_{Hartree} is the Hartree potential, V_{xc} is the exchange-correlation potential, and ε^{KS} ($|\phi^{\text{KS}}\rangle$) are the KS energies (orbitals), respectively. Electron addition or removal processes are then considered as quasiparticle (QP) excitations, described by the one-body Green's function G_1 [29,30]. It can be obtained via a Dyson-type equation of motion, which, in spectral representation, is given by

$$[H_0 + \Sigma(E)]\, G_1(E) = E\, G_1(E), \quad (2)$$

with $H_0 = T_0 + V_{\text{ext}} + V_{\text{Hartree}}$ and with $\Sigma(E)$ an electron self-energy operator that describes the exchange-correlation effects. To obtain a solution to Eq. (2), one often applies the *GW approximation*, in which the self-energy is expressed as

$$\Sigma(\mathbf{r}, \mathbf{r}', \omega) = \frac{i}{2\pi}\int d\omega' G_1(\mathbf{r}, \mathbf{r}', \omega + \omega')W(\mathbf{r}, \mathbf{r}', \omega'). \quad (3)$$

Here, $W(\mathbf{r}, \mathbf{r}', \omega') = \int \varepsilon^{-1}(\mathbf{r}, \mathbf{r}'', \omega')\, v_c(\mathbf{r}'', \mathbf{r}')\, d\mathbf{r}''$ is the screened Coulomb interaction between unit charges at positions $\mathbf{r}$ and $\mathbf{r}'$, with $v_c(\mathbf{r}, \mathbf{r}') = 1/|\mathbf{r} - \mathbf{r}'|$ being the bare Coulomb interaction and $\varepsilon^{-1}(\mathbf{r}, \mathbf{r}'', \omega)$ the inverse of the frequency-dependent dielectric function, calculated in the *random-phase approximation* (RPA) [34]. Within the *GW* approximation, quasiparticle wave functions are expressed in a basis of KS orbitals, which allows calculation of the quasiparticle energies $\varepsilon_i^{\text{QP}}$ from the energy-dependent *GW* Hamiltonian [35,36],

$$H_{ij}^{GW}(E) = \varepsilon_i^{\text{KS}}\delta_{ij} + \left\langle\phi_i^{\text{KS}}\middle|\Sigma(E) - V_{\text{xc}}\middle|\phi_j^{\text{KS}}\right\rangle. \quad (4)$$

Assuming further that $|\phi_i^{\text{QP}}\rangle \approx |\phi_i^{\text{KS}}\rangle$, the quasiparticle energies are determined as

$$\varepsilon_i^{\text{QP}} = \varepsilon_i^{\text{KS}} + \Delta\varepsilon_i^{GW} = \varepsilon_i^{\text{KS}} + \left\langle\phi_i^{\text{KS}}\middle|\Sigma\left(\varepsilon_i^{\text{QP}}\right) - V_{\text{xc}}\middle|\phi_i^{\text{KS}}\right\rangle. \quad (5)$$

Finding the solutions to Eq. (5) requires a self-consistent procedure, as the correction term $\Delta\varepsilon_i^{GW}$ and the nonlocal, energy-dependent microscopic dielectric function calculated within the RPA used in the construction of $\Sigma(E)$ depend on $\varepsilon_i^{\text{QP}}$ [34,37]. In what is known as ev*GW* [31,32,38], we iteratively solve the quasiparticle equations by updating all quantities that depend on the quasiparticle energies, until self-consistency is achieved.

Ground-state calculations including geometry optimizations on the KS-DFT level are performed with the ORCA [39] package using the hybrid Perdew-Burke-Ernzerhof (PBE0) functional [40] and the cc-pVTZ basis [41]. The VOTCA-XTP [32,38] software is used for *GW* steps employing Gaussian-type orbitals as basis functions. An optimized auxiliary basis set [42] is used for resolution-of-identity techniques to efficiently express terms involving four-center Coulomb integrals. The convergence limit for the self-consistent *GW* cycles in the ev*GW* scheme was set to 10^{-5} Hartree (0.272 meV). The number of occupied and unoccupied levels taken into account for the QP calculations is 327. Calculation of the RPA dielectric function requires the full spectrum of the KS states (1385 levels).

B. Calculated single-molecule LUMO energies

Table I gives an overview of the calculated (vertical) energies of the three lowest unoccupied levels of single molecules of α-MADN and β-MADN, as obtained from three methods. We note that a negative value of the LUMO energy, expressed with respect to the vacuum level energy, implies a positive electron affinity. The first row gives, as a reference, the Kohn-Sham DFT result without quasiparticle corrections. The second and third rows give *GW* results, i.e., including

TABLE I. Comparison of the calculated vertical gas-phase energy levels (in eV) for LUMO (L), LUMO+1 (L+1), and LUMO+2 (L+2) of α-MADN and β-MADN, obtained using the PBE0 exchange-correlation functional with the cc-pVTZ basis set, within KS-DFT (KS) and including perturbative quasiparticle corrections from FAA and PPM quasiparticle calculations, respectively. The difference between the latter two is given by $\Delta_{\mathrm{FAA}}^{\mathrm{PPM}}$. All energies are expressed with respect to the vacuum level energy.

	α-MADN			**β**-MADN		
	L	L+1	L+2	L	L+1	L+2
KS	−1.75	−1.20	−1.19	−1.74	−1.23	−1.23
FAA	−0.38	+0.39	+0.41	−0.36	+0.37	+0.36
PPM	−0.23	+0.53	+0.55	−0.21	+0.51	+0.51
$\Delta_{\mathrm{FAA}}^{\mathrm{PPM}}$	−0.15	−0.14	−0.14	−0.15	−0.14	−0.15

quasiparticle corrections, as obtained with a fully analytical approach [31] (FAA) or a generalized plasmon-pole model (PPM) [37] for the frequency integration in Eq. (3), respectively. The FAA is, in principle, an exact form, in which the frequency dependence of the self-energy is expressed in the eigenbasis of the full RPA Hamiltonian in a KS product state basis. Its application to molecules of the size of MADN is computationally extremely demanding due to scaling with N_{b}^6, where N_{b} is the number of basis functions [31]. Use of a PPM, on the other hand, allows for a comparatively fast evaluation of the self-energy, even for larger systems, but can yield deviations of several tenths of an eV from the exact result [31,43].

The results in Table I show the general effect of *GW* corrections to the KS energies. We note a nearly constant shift of $\Delta_{\mathrm{FAA}}^{\mathrm{PPM}} = -0.15$ eV for the three lowest unoccupied energy levels of geometry-optimized α-MADN and β-MADN, respectively. Carrying out *GW* calculations for the 770 molecules in a thin-film morphology with conformational disorder, presented in Sec. III A, is therefore made computationally feasible by using the PPM and by applying to each molecule-specific value of the calculated LUMO energy the above-mentioned constant energy shift $\Delta_{\mathrm{FAA}}^{\mathrm{PPM}}$.

Previous studies on anthracene have shown that the inclusion of zero-point vibrational energy (ZPVE) effects influences its electron affinity of the order of one-tenth of an eV [44]. As both MADN derivatives contain an anthracene core, similar effects on the LUMO energies can be expected here. We therefore determine ZPVEs for neutral and anionic molecules based on DFT and find a reduction of the LUMO energy of $\Delta_{\mathrm{ZPVE}} = -0.11$ eV [45]. The intramolecular contribution of level ℓ to the unoccupied quasiparticle energy for each molecule M, $\varepsilon_{\ell,M}^{\mathrm{intra}}$, is thus obtained by performing *GW* calculations with the PPM and by correcting the effects of the PPM and the ZPVE,

$$\varepsilon_{\ell,M}^{\mathrm{intra}} = \varepsilon_{\ell,M}^{\mathrm{intra,PPM}} + \Delta_{\mathrm{FAA}}^{\mathrm{PPM}} + \Delta_{\mathrm{ZPVE}}. \tag{6}$$

C. QM/MM polarizable embedding with long-range interactions

Amorphous thin-film geometries of α-MADN and β-MADN were generated using a simulated deposition protocol based on classical force fields. See Ref. [7] for details. The final freestanding morphologies contain 770 molecules. They are periodic in the x and y directions, with box lengths of approximately 10 nm. After removal of an artificially dense fixed bottom layer representing a substrate for the deposition, the films extend about 8 nm in the z direction. The simulations yield molecular densities of 1.52×10^{27} m^{-3} and 1.49×10^{27} m^{-3} for α-MADN and β-MADN, respectively.

The single-molecule (gas-phase) quasiparticle energies as determined in the previous section are modified due to intermolecular interactions by using an embedding scheme, within which embedding-induced corrections to the intramolecular *GW* energies are evaluated in a coupled quantum-classical (QM/MM) procedure [7,38,46,47]. The MM model provides a classical representation of the molecular electrostatic potential, consisting of atomic static and induced multipole moments. Within the *subtractive scheme* that is used in this work for coupling the QM and MM regions, the same type of classical representation is also used for the molecules in the QM region. These representations are different for the ground state ($s = n$) and the negatively charged states ($s = \ell$). A purely classical energy correction $E_{\mathrm{MM}}^{(\ell)} - E_{\mathrm{MM}}^{(n)}$ is added to the *GW* gas-phase energies. To parametrize the model, we limit the static moments to partial charges which are obtained from a CHELPG (charges from electrostatic potentials using a grid-based method) fit to the neutral and charged molecule's electrostatic potential [48], respectively. The atomic polarizabilities are determined from the molecular polarizability tensors in the neutral and charged states. The latter need to be calculated numerically from the second derivative of the total energy with respect to externally applied electric fields.

Within this work, the QM region includes only a single molecule. Thin films of α-MADN and β-MADN show a spatially inhomogeneous interaction due to structural anisotropy that results in partially oriented molecular dipole moments. A proper treatment of the MM regions requires, therefore, a scheme in which long-range electrostatic interaction effects are included. That is accomplished by using an infinite periodic embedding that is based on the traditional classical Ewald summation method [49,50]. In this so-called polarizable *GW*/pMM scheme, the neutral system provides a two-dimensional (2D) periodically polarized background to which (when considering the charged state) a localized nonperiodic excitation is added. The excitation is located within a polarizable cutoff region around the QM region of interest [7,47,51,52], with a cutoff radius of 6 nm. To accommodate such a large cutoff (larger than half of the box size in the x and y directions), we first construct a 2×2 supercell. The final embedded QM/MM quasiparticle energies are given by

$$\varepsilon_{\ell,M}^{\mathrm{QM/MM}} = \varepsilon_{\ell,M}^{\mathrm{intra}} + \varepsilon_{\ell,M}^{\mathrm{inter}} = \varepsilon_{\ell,M}^{\mathrm{intra,PPM}} + \Delta_{\mathrm{FAA}}^{\mathrm{PPM}} + \Delta_{\mathrm{ZPVE}} + E_{\mathrm{MM}}^{(\ell,M)} - E_{\mathrm{MM}}^{(n,M)}. \tag{7}$$

In this expression, the terms without molecule index M ($\Delta_{\mathrm{FAA}}^{\mathrm{PPM}}$ and Δ_{ZPVE}) are determined on the vacuum single-molecule level, whereas all terms with a molecule index are specific to this molecule and its disordered environment. Detailed expressions for the classical energies $E_{\mathrm{MM}}^{(s)}$ and for the static atomic multipole moments that determine these interaction

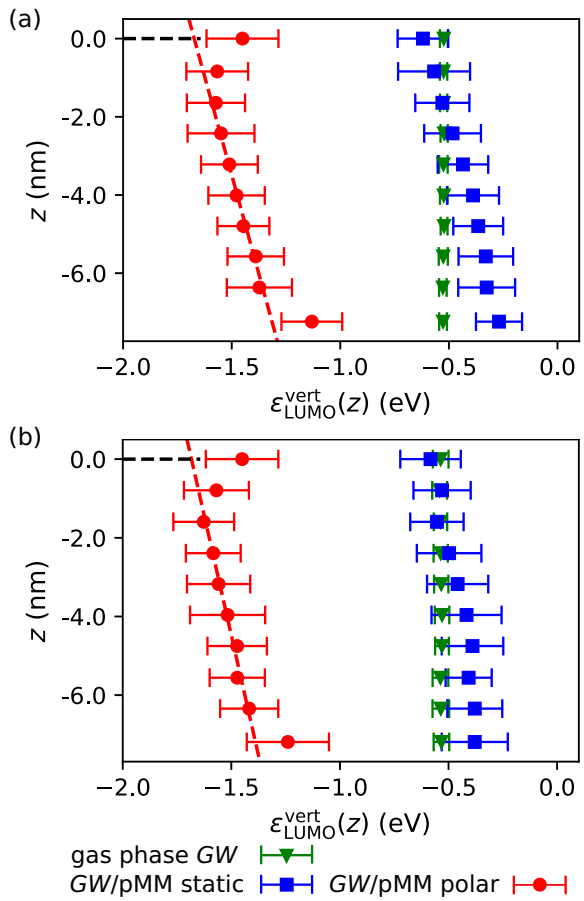


FIG. 2. Layer-resolved distributions of *vertical* quasiparticle LUMO energies (in eV) as obtained from gas phase *GW* (green), static (blue), and polarizable (red) *GW*/pMM calculations for thin films of (a) α-MADN and (b) β-MADN. The error bars show the distribution widths ($\pm\sigma_e$). The bulk value of $\varepsilon^{\text{vert}}_{\text{LUMO}}$ is obtained by an extrapolation of the *GW*/pMM polar values of $\varepsilon^{\text{vert}}_{\text{LUMO}}(z)$ to the $z = 0$ plane (dashed lines). The LUMO energies are expressed with respect to the vacuum level energy.

energies have been given in Ref. [7] [Eqs. (7) and (8), respectively] and in Ref. [23] (Secs. 3.3.2 and 3.3.3).

III. THEORETICAL ELECTRON AFFINITY DISTRIBUTIONS AND LEIPS SPECTRA

A. Layer-resolved vertical unoccupied electronic structure in molecular thin films

Figure 2 shows the calculated z-layer averaged dependence of the vertical (nonadiabatic) LUMO energies in the 8 nm thin-film morphologies of α-MADN [Fig. 2(a)] and β-MADN [Fig. 2(b)], obtained from gas phase *GW* (green), static (blue), and polarizable (red) *GW*/pMM calculations, respectively. Each layer contains 77 molecules. The energy is given with respect to the vacuum level energy, ε_{vac}. These vertical energies include the effects of (fast) electronic relaxation when adding an electron to the system, as in a LEIPS experiment. A methodology for calculating the energy shift due to vibronic relaxation, which is a slower process, is presented in Sec. III B. The relation with the adiabatic energies will be discussed in Sec. III E. In the figure, the distributions of the energies in a single layer are represented by violin plots, with the symbols indicating their median. The disorder in the static and polar *GW*/pMM LUMO energies, shown in Fig. 2, is dominated by effects from intermolecular interactions. Conformational disorder, which already leads to distributions of $\varepsilon^{\text{intra}}_{\ell,M}$ (the energies without embedding) is found to be negligibly small: it only broadens the vacuum quasiparticle energies of α-MADN (β-MADN) by 0.01 (0.03) eV. For α-MADN, the disorder is, in the polar (static) case, 0.12–0.17 eV (0.11–0.17 eV), which is slightly smaller than the corresponding values of 0.16–0.20 eV (0.11–0.17 eV) for β-MADN.

Whereas the static and polarizable calculations lead thus to quite similar disorder energies, there are clear differences in the resulting mean/median energies and their dispersion/band shape along the z direction perpendicular to the film. Within static *GW*/pMM (blue symbols in Fig. 2), there is an almost linear energy-level gradient due to the interactions with a net dipole moment in the films formed during the deposition process [7]. Such a "spontaneous orientation polarization" effect is well known for organic semiconductors [53,54]. The energy-level gradient is larger for α-MADN due to a higher net dipole moment compared to β-MADN (62.1 vs 32.9 D for the simulation boxes considered). Including polarizable interactions in polar *GW*/pMM (red symbols in Fig. 2) lowers the LUMO energies in the center of the films by nearly 1 eV, e.g., to -1.52 eV for α-MADN and to -1.45 eV for β-MADN in the $z = 6.2$ nm layer. At the interface with the vacuum at the top and the bottom of the freestanding films, the effects of polarization are smaller than in the bulk of the films, as the molecules are surrounded by less polarizable material. For both isomers of MADN, the calculated polarization energy is, at the vacuum surface, on average, reduced by 0.20 eV. A similar reduction has been observed experimentally for various other organic thin-film materials [55,56]. As a consequence, the z dispersion resembles a U shape, with energy-level bending towards less negative energies at the interfaces. Note that this shape is not completely symmetric due to the morphological details and structural disorder. Also a slight "tilt" is visible from the interactions with the net dipole moment as in the static case.

The bulk values of the vertical LUMO energies may be deduced from the z-resolved vertical LUMO energies by extrapolation to the $z = 0$ nm plane (dashed lines in Fig. 2). These energies are (-1.64 ± 0.13) eV and (-1.65 ± 0.14) eV for α-MADN and β-MADN, respectively. The bulk values of their Gaussian distribution widths (standard deviation σ) are 0.14 eV and 0.19 eV, respectively. We note that on first sight, obtaining a "bulk" LUMO energy by extrapolation to the surface plane might sound contradictory. However, it should be realized that (i) the deviating LUMO energies at the vacuum surface are irrelevant to applications of the simulation results in fully buried OLED layer stacks, so that a procedure should be used that eliminates their effect, and (ii) in a strict manner, the "ionization and electron affinity of a solid are defined at, and only at, the surface of the material" [57]. This motivates the use of the extrapolation procedure. In OLED device simulations, the proper depth gradient of the HOMO and LUMO energies within the bulk of the layers is then obtained by adding the electrostatic field that arises

from the partially oriented dipole moments, as discussed in Ref. [58].

The shape of LEIPS spectra is also determined by spectral contributions from higher-energy states. The LUMO+1 and LUMO+2 states are, for both isomers, found to be almost degenerate, with vertical energies that differ by 0.01–0.02 eV with an average of 0.68 eV above that of the LUMO. The energies of the LUMO+3 ($\ell = 4$) and higher states are approximated by shifting the values of the vertical LUMO energies, obtained from the *GW*/pMM calculations, by the energy difference $\varepsilon_\ell^{\mathrm{QP}} - \varepsilon_{\mathrm{LUMO}}^{\mathrm{QP}}$ that has been obtained from the vacuum calculation. For $\ell = 4$–6 and for α-MADN (β-MADN), these shifts are 1.23 (1.22), 1.43 (1.41), and 1.58 (1.57) eV, respectively. Figure S1 of the Supplemental Material [25] shows the wave functions for these states. For both isomers, the LUMO states are localized on the anthracene cores of the molecule. The LUMO+1 and LUMO+2 states are located on the naphthyl side groups, whereas for the LUMO+3 states, the wave function is of a more mixed (core/side group) character.

B. Vibronic relaxation

When performing a LEIPS experiment, in which an electron is added to the system on a femtosecond timescale, the emission of a photon is accompanied by creating vibrational excitations. As a result, the spectral response is broadened by a state- and molecule-dependent function $S_{\ell,M}^{\text{el-vib}}(\omega)$ that includes the effect of the intramolecular reorganization process upon charge addition and the associated shift and lineshape broadening due to electron-vibration coupling. It is obtained using the full-quantum (FQ) approach for intermolecular charge transfer [59], which approximates the potential energy surface of the excited molecule in the independent mode displaced harmonic-oscillator model [60]. The approach utilizes the Franck-Condon principle and includes coupling to all vibrational modes. The methodology is made possible by the localized nature of the electronic and vibrational states in the disordered materials that have been studied, which simplifies the theory as compared to that for electron-phonon interactions in crystalline materials. It has been applied earlier when analyzing the shape of UPS spectra of α-MADN and β-MADN [7]. Specifically, the spectral shape due to coupling of the incoming electrons with vibrational modes k with an energy $\hbar\omega_k$ and a coupling energy λ_k is given by

$$S_{\ell,M}^{\text{el-vib,FQ}}(\hbar\omega) = \frac{1}{2\pi\hbar}\int_{-\infty}^{+\infty} e^{i\omega t} e^{-F_{\ell,M}(0)} e^{F_{\ell,M}(t)}\, dt, \quad (8)$$

where

$$F_{\ell,M}(t) = \sum_k \frac{\lambda_k^{\ell,M}}{\hbar\omega_k}\left[\coth\left(\frac{\hbar\omega_k}{2k_{\mathrm{B}}T}\right)\cos(\omega_k t) + i\sin(\omega_k t)\right], \quad (9)$$

with k_{B} the Boltzmann constant and T the temperature. The underlying assumptions are that (i) the ground- and excited-state potential energy surfaces are harmonic and (ii) no vibrational frequency alteration or normal mode rotation occurs in the excited state. Only the ground-state vibrational mode frequencies ω_k and the gradient of the total energy for the excited system in the ground-state geometry with respect to the phonon mode coordinates q_k, $\partial E^{(\ell,M)}/\partial q_k$, need to be evaluated. The mode-specific couplings are then determined as $\lambda_k^{\ell,M} = \frac{1}{2}\partial E^{(\ell,M)}/\partial q_k$. For calculating LEIPS spectra, we determine these gradients with numerical differences for the LUMO state and the two degenerate LUMO+1 and LUMO+2 states in the optimized ground-state geometry and employ the same $S_\ell^{\text{el-vib,FQ}}(\omega)$ for all molecules M. As the S functions for these three states are found to be almost indentical, the S function for the higher-energy states ($\ell = 4$–6) that are included when calculating the LEIPS spectra will be taken equal to that of the LUMO state.

The sum $\lambda_{\mathrm{tot}}^{\ell,M} = \sum_k \lambda_k^{\ell,M}$ is the total reorganization energy of state ℓ. The total reorganization energy for the LUMO state will be denoted as λ_{reorg}. The relation between the vertical and adiabatic LUMO energies is

$$\varepsilon_{\mathrm{LUMO}}^{\mathrm{vert,bulk}} = \varepsilon_{\mathrm{LUMO}}^{\mathrm{ad,bulk}} + \lambda_{\mathrm{reorg}}. \quad (10)$$

We find $\lambda_{\mathrm{reorg}} = 0.18$ eV and 0.14 eV for α-MADN and β-MADN, respectively, which is slightly smaller than the value of 0.21 eV for holes in both isomers [7]. The calculated full width at half maximum (FWHM) of the S functions is 0.36/0.32 eV and 0.34/0.25 eV for the LUMO/LUMO(+1, +2) for α-MADN and β-MADN, respectively. The shape of these response functions is slightly skewed, with a somewhat elongated high-energy tail. The S functions have standard deviations σ_{vibr} of 0.16/0.14 eV and 0.15/0.12 eV for the LUMO/LUMO(+1, +2) for α-MADN and β-MADN, respectively. For ideal Gaussian distributions, the standard deviation is a factor $\sqrt{8\ln 2}$ larger than the FWHM. The actual ratios are close to this factor. Within the classical Marcus theory, the width (standard deviation) of the S function would be expected to be $\sqrt{2\lambda_{\mathrm{reorg}}k_{\mathrm{B}}T}$. The calculated widths of 0.12–0.16 eV, which have been obtained from a full-quantum approach that includes contributions of high-energy modes (with energies well above $k_{\mathrm{B}}T$), are somewhat larger than the classical value of ≈0.11 eV.

C. Charging: Effect on the LUMO energy profile

In practical LEIPS experiments, the incident current density J_{in} is taken to be in the range 0.01 to 0.1 A/m^2 [61], so that a sufficiently large count rate is obtained while limiting the spectral changes due to charging. We examine, in this section, how charging could still affect the shape of the LUMO energy profile. We remark that giving a full analysis of the results of LEIPS experiments under realistic experiment-induced charging conditions is beyond the scope of this work, and that the main goal is to indicate the charging-induced modifications to the spectral shifts and broadenings. An experimental methodology that is used to reduce the sensitivity to charging is discussed in Sec. IV.

Under steady-state conditions, the areal density of electrons in the film, n_{A}, is determined by the average layer-thickness-dependent time $\bar{t}_{\mathrm{esc}}$ during which an electron stays in the film before escaping to the substrate by a drift and diffusion process, so that

$$n_{\mathrm{A}} = \bar{t}_{\mathrm{esc}}\frac{J_{\mathrm{in}}}{e}, \quad (11)$$

assuming that all incident electrons are absorbed. We will also assume here that absorption occurs at random molecules in the film and that it is followed by fast relaxation process to

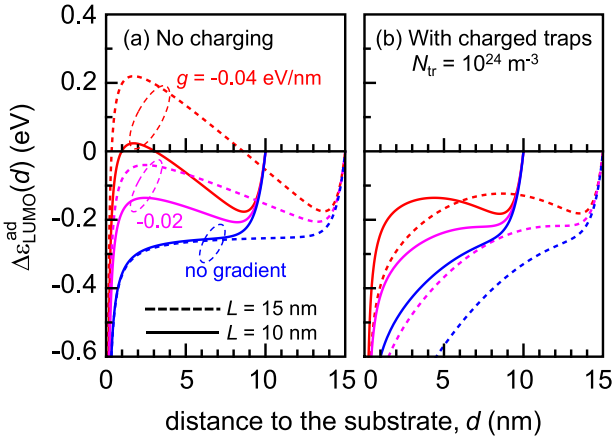


FIG. 3. LUMO energy profile in 10 and 15 nm films on a metallic substrate without an electrostatic potential gradient in the bulk of the films (blue "no gradient" curves) and with $g = -0.02$ and -0.04 eV/nm (magenta and red curves). (a) For a noncharged film. (b) For films containing a uniform distribution of trapped charges with a density of 10^{24} m^{-3}. The shapes of the profile are as described by Eqs. (12) and (15), with $\varepsilon_r = 3$ and with a surface effect contribution as obtained in Sec. III A.

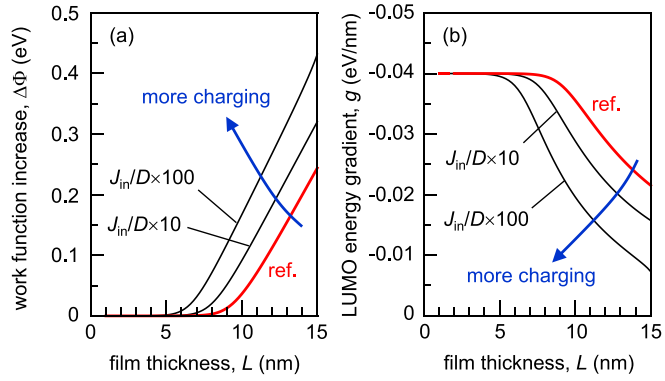


FIG. 4. Self-consistently calculated film-thickness dependence of the effects of charging in a LEIPS experiment for a reference case (red thick curves) with an incident electron current density $J_{in} = 0.01$ A/m^2 and an electron diffusion coefficient $D = 10^{-13}$ m^2/s, and for cases with a 10-fold- and 100-fold-larger $J_{in}D$ product (thin black curves), leading to more charging. (a) Work function increase. (b) Change of the LUMO energy gradient in the bulk of the films.

the LUMO state of that molecule. The average escape time is then determined by the LUMO energy profile in the film, which may be defined as the difference between the average adiabatic LUMO energy at a distance d from the substrate interface and the value at the vacuum interface,

$$\begin{aligned}\Delta\varepsilon^{\rm ad}_{\rm LUMO}(d) &\equiv \varepsilon^{\rm ad}_{\rm LUMO}(d) - \varepsilon^{\rm ad}_{\rm LUMO}(L)\\ &= -g(L-d) - \frac{1}{16\varepsilon_0\varepsilon_r}\frac{e}{d} + \Delta\varepsilon_{\rm surf}(d)\\ &\quad + \Delta\varepsilon_{\rm ch}(d),\end{aligned} \tag{12}$$

with L the film thickness. The energies are expressed in units of eV and all other quantities are expressed in SI units. The profile contains contributions from (i) the potential gradient g (which is about -0.04 eV/nm for the two isomers of MADN), (ii) the image potential contribution near the substrate surface (with ε_0 the vacuum dielectric permittivity and ε_r the relative dielectric constant; see, e.g., Ref. [62]), (iii) the deviating LUMO energy near the vacuum surface (see Fig. 2), and (iv) the shift due to charging. Figure 3(a) shows, as an example, the potential profile without charging for 10 and 15 nm films and for various values of the gradient. For these films, a gradient of -0.04 eV/nm is seen to lead to a deep potential well, close to the vacuum interface. Absorption of the incident electrons is expected to give rise to charge accumulation in a relatively thin zone around the bottom of the well, at a small distance $\delta_{\rm surf}$ from the vacuum interface. From Eq. (11), this leads, for $d < L - \delta_{\rm surf}$, to a near-linear charging contribution,

$$\Delta\varepsilon_{\rm ch}(d) = -\frac{J_{\rm in}\bar{t}_{\rm esc}}{\varepsilon_0\varepsilon_r}(L - \delta_{\rm surf} - d), \tag{13}$$

to the potential profile that counteracts the gradient contribution. The steady-state potential profile can then be obtained using Eqs. (12) and (13) after self-consistently calculating $\bar{t}_{\rm esc}$.

For a LUMO energy profile such as shown in Fig. 3, we find from drift-diffusion simulations (see Sec. S3 in the Supplemental Material [25]) that $\bar{t}_{\rm esc}$ is, to a good approximation, given by

$$\bar{t}_{\rm esc}(L) \approx \frac{2\times10^{-18}}{D}\exp\left[\frac{|g|(L - \delta L - \delta_{\rm surf} - \delta_{\rm ip})e}{k_{\rm B}T}\right], \tag{14}$$

with D the diffusion coefficient, expressed in units of m^2/s, $\delta_{\rm surf} = 1.8$ nm, δL an effective reduction of the film thickness due to the discrete nature of the molecular sites, approaching a value of 1 nm for large gradients $|g|$, and $\delta_{\rm ip}$ an effective reduction of the width of the potential well due to the image potential (ip) effect which is approximately equal to 3 nm for $g = -0.04$ eV/nm. The electron diffusion coefficient can be estimated from the measured mobility μ that follows from time-of-flight experiments [10], using the Einstein equation $D = (k_{\rm B}T/e)\mu$ and after extrapolation to zero applied field. Such a procedure would, for both isomers of MADN, lead to $D \approx (0.5\text{–}1.0)\times10^{-13}$ m^2/s at room temperature. From three-dimensional kinetic Monte Carlo (3D-KMC) simulations, we find that the dependence of the diffusion coefficient on the LUMO disorder energy is consistent with the Gaussian disorder model (GDM) [63] (see Sec. S4 of the Supplemental Material [25]).

Figure 4 shows, for a material with $g = -0.04$ eV/nm, the self-consistently calculated effect of charging as a function of the layer thickness on the work function [Fig. 4(a)] and on the LUMO energy gradient in the bulk of the film [Fig. 4(b)]. The red-colored reference curves have been obtained for $J_{\rm in} = 0.01$ A/m^2 and $D = 10^{-13}$ m^2/s. The work function is for 10 and 15 nm films found to increase by 0.04 and 0.24 eV, respectively, and the potential gradient in the bulk of the film decreases then from -0.04 eV to -0.036 and -0.022 eV, respectively. For a 15 nm film, $n_{\rm A}$ is, under these conditions, about 2×10^{15} m^{-2} (mole fraction of $\sim$0.2%), and the potential profile shifts then from the red-colored to almost the magenta-colored dashed curve in Fig. 3(a). Such a change has to be taken into account when predicting the shape of LEIPS spectra. The effect of charging increases with an increasing

ratio J_{in}/D. The black curves in Fig. 4 show results for 10-fold and 100-fold increased values of this ratio. Even though clear changes are seen, the sensitivity to such huge changes of J_{in} or D is relatively small. That is due to a strong negative feedback, caused by the opposing effects of the intrinsic gradient g and the charging-induced gradient that is given by Eq. (13).

We remark that this analysis of the effects of charging should be refined in two ways. First, charging not only changes the average LUMO energy profile, but also contributes to the spectral distribution width. The standard deviation of this contribution, σ_{ch}, is, for the reference case that has been studied in Fig. 4 with $L = 15$ nm, equal to about 0.12 eV near the vacuum surface, decreasing in proportion to the distance d towards the substrate surface (see Sec. S5 of the Supplemental Material [25]). Second, we need to consider the possible role of charging due to filling of deep electron traps. For organic semiconductors with a relatively shallow LUMO energy, strong experimental evidence for the presence of deep traps has been obtained from charge transport studies [64–68]. The trapping is attributed to the almost unavoidable presence of water or oxygen molecules [67,68], with effective LUMO energies of approximately -3.5 eV [67]. For small-molecule organic semiconductors with large energy gaps, the trap density N_{tr} is typically $(1\text{–}5)\times 10^{24}$ m^{-3} [64,66,67,69], corresponding to a mole fraction of about 0.1–0.5%. A LEIPS experiment is expected to lead to fast filling of such deep traps, irrespective of the incident current density. The filling is expected to be almost permanent, in view of the large trap depth, the small trap concentration, and the absence of a large electrostatic field in the bulk of the film. In the remainder of this section, we briefly study the consequences of this additional charging effect. At present, we do not have sufficient information about the density and depth of such traps in films of α-MADN and β-MADN. However, we will argue in Sec. IV B that the LEIPS studies provide evidence of an important effect on the spectral widths.

Within a continuum model that assumes a spatially uniform volume density N_{tr} of trapped electrons, the additional electrostatic shift of the LUMO energy profile in the film would be

$$\Delta\varepsilon_{\text{ch,tr}}(d) = -\frac{e}{2\varepsilon_0\varepsilon_{\text{r}}} N_{\text{tr}}(L-d)^2. \tag{15}$$

This contribution to the variation of the adiabatic average LUMO energy across the film thickness can be sizable. The work function increase is equal to $|\Delta\varepsilon_{\text{ch,tr}}(0)|$. For a 10 nm film, for example, with $N_{\text{tr}} = 10^{24}$ m^{-3} and $\varepsilon_{\text{r}} = 3$, an increase of 0.30 eV would be expected. Figure 3(b) shows the effect of such a density of deep traps on the LUMO energy profile, for 10 and 15 nm films and for various values of the bulk LUMO energy gradient. The figure shows that for a gradient of -0.04 eV (full and dashed red curves), the depth of the potential well near the vacuum surface has decreased strongly as compared to the situation without traps [Fig. 3(a)]. The role of charge accumulation in intrinsic LUMO states will therefore be much smaller than in the absence of deep electron traps. For materials without an intrinsic LUMO energy gradient (blue curves), the figure even suggests that charge accumulation in regular LUMO states could be almost absent due to a strong internal field, leading to fast drift of injected charges to the substrate. From 3D-KMC simulations, we indeed find a strong reduction of the average escape time when adding a small concentration of traps (see Sec. S4 of the Supplemental Material [25]). Numerical calculations show that for $N_{\text{tr}} = 10^{24}$ m^{-3}, the contribution of the trapped charges to the stochastic variation (standard deviation, $\sigma_{\text{ch,tr}}$) of the site-resolved LUMO energy is, near the vacuum surface, about 0.1 eV (see Sec. S5 of the Supplemental Material [25]), where the variation of this distribution width on the layer thickness, trap density, and position in the film is studied.

In summary, film charging due to electrons that reside in intrinsic LUMO states or in deep trap states can significantly affect the LEIPS spectra. The precise sensitivity to changes of the LUMO energy profile depends on the probing depth, which is studied in the next section.

D. Surface sensitivity

The effective probing depth in a LEIPS experiment is determined by elastic and inelastic scattering processes. The distribution of depths that the incoming electrons reach before having lost part of their energy in an inelastic scattering event is conventionally expressed in terms of an exponential extinction function, $f(z) = \exp(-|z|/\Lambda)$, with $|z|$ the distance to the film-averaged vacuum interface and Λ the electron attenuation length (EAL). The EAL is determined by the interplay between inelastic scattering due to electron-hole pair and plasmon creation, with a mean free path λ_{in}, and quasi-elastic scattering (deflections that lead to momentum randomization), characterized by the transport mean free path λ_{tr}. When $\lambda_{\text{tr}} > \lambda_{\text{in}}$, the EAL may be expressed as

$$\Lambda \approx \frac{\lambda_{\text{in}}\lambda_{\text{tr}}}{\lambda_{\text{in}} + \lambda_{\text{tr}}}, \tag{16}$$

whereas $\Lambda \approx \lambda_{\text{tr}}$ for $\lambda_{\text{tr}} \ll \lambda_{\text{in}}$ [70]. The LEIPS spectrum will be obtained using an effective surface density of states [SDOS, $\mathcal{D}(E)$] of unoccupied states that is defined as

$$\mathcal{D}(E) = \sum_{\ell,M} f(d_M)\delta\big(E - \varepsilon_{\ell,M}^{\text{QM/MM}}\big). \tag{17}$$

Here, the summation is over all ℓth energy levels of all molecules M in the system, $\varepsilon_{\ell,M}$, as calculated from GW/pMM, and $f(z_M)$ is the extinction function at the location of molecule M.

Formally, the energy dependence of λ_{in} can be deduced from the contribution of electronic inelastic scattering to the electron energy-loss function (see, e.g., Ref. [71]). For a large range of materials, the energy dependence has been found to follow a "universal curve" [72], which suggests that for energies below 10 eV, the inelastic mean free path in organic materials can be in the range of 1–100 nm. That is supported by upper-limit estimates for MADN, based on the random-phase approximation using GW energies (see Supplemental Material of Ref. [7]). However, internal photoemission [73], photoelectron yield [74], and electron-electron energy-loss coincidence spectroscopy experiments [70] suggest that for the low kinetic energies of the incident electrons in LEIPS experiments, well below 10 eV, the EAL is smaller than the value of λ_{in} that would follow from the universal curve, limiting the EAL to values in the range 1–10 nm for electron energies that are used in LEIPS experiments. In Ref. [73], this

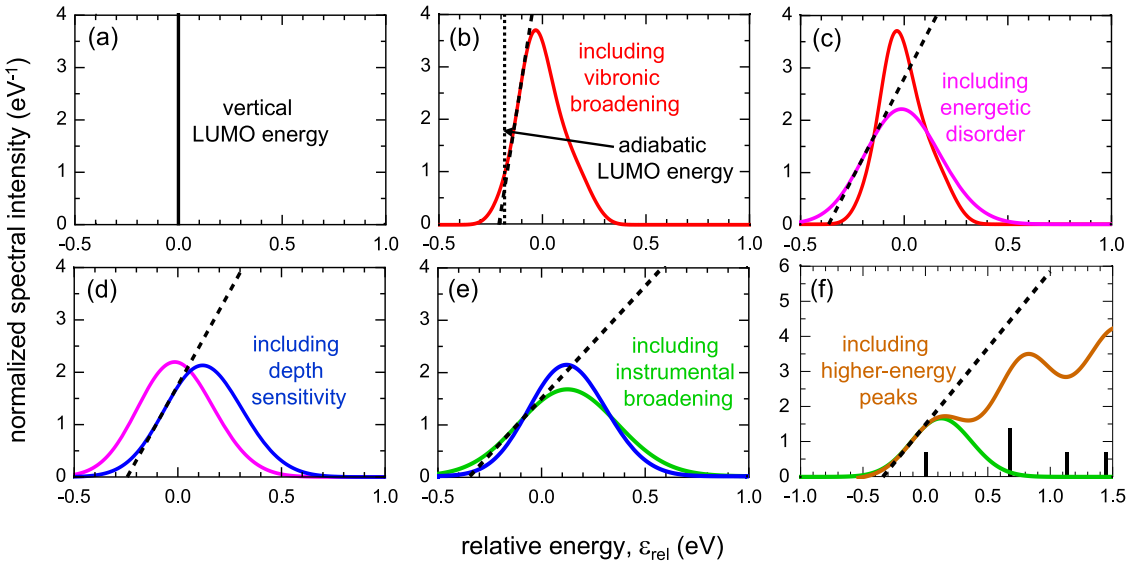


FIG. 5. Schematic stepwise calculation of normalized LEIPS spectra from results of quantum-chemical simulations, using parameter values that are typical for the LEIPS studies of α-MADN and β-MADN that are presented in this work. (b)–(f) The cumulative effect of carrying out steps 1–5 that have been described in Sec. III E, starting with a delta-function-shaped peak at the calculated bulk value of (a) the vertical LUMO energy, $\varepsilon_{\mathrm{LUMO}}^{\mathrm{vert,bulk}}$, obtained using Fig. 2 (see Sec. III A). The spectra are given as a function of $\varepsilon_{\mathrm{rel}} \equiv \varepsilon - \varepsilon_{\mathrm{LUMO}}^{\mathrm{vert,bulk}}$. In (c)–(f), the result from the previous step is also shown. Note the adapted scales of (e) and (f). Dashed lines are the tangents to the lowest-energy inflection points. The zero-intensity points of the tangents, for each spectrum, give the spectral onset energy. When including steps 1–4, the onset energy is given by Eq. (19). (f) Step 5 leads to a further small shift. The vertical dotted line in (b) is located at the adiabatic LUMO energy [$\varepsilon_{\mathrm{rel}} = -\lambda_{\mathrm{reorg}}$; see Eq. (10)].

has been attributed to momentum relaxation due to vibrational scattering. Developing proper theoretical models that could provide λ_{in} and λ_{tr} is hampered by the amorphous nature of the materials that have been studied. It is not evident to what extent models that assume a delocalized electronic structure can appropriately describe the initial states in the film, whereas such a description is well known to be entirely inadequate for describing the electronic structure of the final states close to the LUMO. Concerning the role of vibrational scattering, we remark that a study of the contributions of vibrational modes to the relative permittivity does not provide an indication that the strength of vibrational scattering in α-MADN and β-MADN would be exceptionally large (see Sec. S2 of the Supplemental Material [25]). We will therefore assume in our analyses of LEIPS spectra that $\Lambda \sim 4$ nm, near the center of the range of experimental values for various systems that has been mentioned above. The sensitivity of the spectral onset energy is found to be small when varying Λ in the range 2–10 nm.

E. Contributions to LEIPS spectra

Before giving the final theoretical spectra for α-MADN and β-MADN, in Sec. III F, we summarize here how such spectra can be obtained from the theoretical results that have been presented in Secs. III A–III D. We remark that the LEIPS spectra that will be presented in this work have been measured using a procedure that compensates, at least in part, for the effect of charging due to the electron beam [75], using low-energy electron transmission (LEET) measurements (see Sec. IV A). We will not include charging effects here, but will discuss their effects on the LUMO energy profile and the peak broadening when comparing, in Sec. IV B, the experimental and theoretical spectra.

Figure 5 shows the sequence of steps that leads from the bulk value of the vertical LUMO energy [Fig. 5(a)] to the final spectrum [Fig. 5(f), orange curve]. In the figure, $\varepsilon_{\mathrm{rel}}$ is the energy with respect to $\varepsilon_{\mathrm{LUMO}}^{\mathrm{vert,bulk}}$. These steps involve the following:

(1) Broadening due to the excitation of vibrational modes as a result of the nonadiabaticity of the process, as discussed in Sec. III B [Fig. 5(b)].

(2) Broadening due to energetic disorder [Fig. 5(c)]. In the figure, broadening with a disorder energy of $\sigma_{\mathrm{dis}} = 0.14$ eV is shown, as for α-MADN.

(3) Shift and broadening due to the z dependence of the layer-averaged LUMO density of states (from Sec. III A) in the experimentally probed surface zone [Fig. 5(d)]. Contributions near the surface plane with an exponentially decreasing weight, determined by an electron attenuation length $\Lambda =$ 4 nm, have been included (see Sec. III D). The overall upward shift of the spectrum is then about 0.15 eV.

(4) Experimental resolution broadening [Fig. 5(e)], for the case of Gaussian broadening with a width (standard deviation) of $\sigma_{\mathrm{instr}} = 0.13$ eV (the best resolution used in the experiments; see Sec. IV).

(5) Addition of the spectral contributions due to higher-energy states [Fig. 5(f)]. In the figure, contributions from the six lowest-energy states (thin vertical lines; see Sec. III A) are included, assuming equal transition matrix elements.

The spectral onset energy is commonly defined by extrapolating the tangent through the low-energy inflection point of a spectrum to the baseline (dashed lines in Fig. 5). It may be seen from Fig. 5(d) that before including the instrumental

broadening, the onset energy is, in this case, less than 0.1 eV different from the adiabatic LUMO energy [vertical dotted line in Fig. 5(b), −0.18 eV] for α-MADN. However, this near coincidence is somewhat fortuitous, as the onset energy depends on the three material-specific contributions that are included in Figs. 5(b)–5(d). Figure 5(e) shows that after including the experimental broadening, the onset energy is about 0.35 (0.17) eV lower than the vertical (adiabatic) LUMO energy. We note that Fig. 5 gives only a schematic overview and that the spectra that will be presented and analyzed in Sec. III F are based on the actual simulation data.

The view on the spectral shape that is presented in Fig. 5 may be generalized as follows. When approximating the vibronic, disorder, and instrumental resolution effects by assuming a Gaussian distribution, and when approximating the effect of the surface sensitivity as the combined effect of an energy shift $\Delta\varepsilon^{\mathrm{surf,av}}_{\mathrm{LUMO}}$ and a Gaussian broadening with a width σ_{surf}, the total broadening of the spectrum from a single state is approximately

$$\sigma_{\mathrm{tot}} \approx \sqrt{\sigma^2_{\mathrm{vibr}} + \sigma^2_{\mathrm{dis}} + \sigma^2_{\mathrm{surf}} + \sigma^2_{\mathrm{instr}}}. \tag{18}$$

In the absence of spectral contributions due to higher-energy states, the relationship between the adiabatic bulk value of the LUMO energy and the spectral onset energy is then

$$\varepsilon^{\mathrm{single-state}}_{\mathrm{LEIPS,onset}} \approx \varepsilon^{\mathrm{vert,bulk}}_{\mathrm{LUMO}} + \Delta\varepsilon^{\mathrm{surf,av}}_{\mathrm{LUMO}} - 2\sigma_{\mathrm{tot}}. \tag{19}$$

Adding contributions from higher-energy states for which the total disorder width is the same will, in general, give rise to a positive shift of the onset energy, $\Delta\varepsilon^{\mathrm{multi-state}}_{\mathrm{LEIPS,onset}}$ (see Sec. S6 of the Supplemental Material [25]). Figure 5(f) shows that for this example, such contributions are only expected to blur the separate state-specific contributions. The resulting shift of the onset energy is for the conditions that have been assumed to be very small. From Eqs. (10) and (19), the relationship between the adiabatic bulk value of the LUMO energy and the spectral onset energy is then

$$\varepsilon^{\mathrm{ad,bulk}}_{\mathrm{LUMO}} \approx \varepsilon^{\mathrm{full-spectrum}}_{\mathrm{LEIPS,onset}} - \lambda_{\mathrm{reorg}} - \Delta\varepsilon^{\mathrm{surf,av}}_{\mathrm{LUMO}} + 2\sigma_{\mathrm{tot}} - \Delta\varepsilon^{\mathrm{multi-state}}_{\mathrm{LEIPS,onset}}. \tag{20}$$

This expression generalizes the results of this study by showing how the onset energy from a LEIPS experiment is related to the bulk value of the adiabatic LUMO energy that is needed as an input in OLED device simulations. Charging effects will not change the general form of this expression, but can affect $\Delta\varepsilon^{\mathrm{surf,av}}_{\mathrm{LUMO}}$ and σ_{tot}.

We remark that the methodology that has led to Eq. (20) is analogous to the methodology that has been used in Ref. [7] for analyzing UPS spectra of α-MADN and β-MADN. In general, the relation between the onset energy that is obtained using the tangent method from UPS spectra and the bulk value of the adiabatic HOMO energy is

$$\varepsilon^{\mathrm{ad,bulk}}_{\mathrm{HOMO}} \approx \varepsilon^{\mathrm{full-spectrum}}_{\mathrm{UPS,onset}} + \lambda_{\mathrm{reorg}} - \Delta\varepsilon^{\mathrm{surf,av}}_{\mathrm{HOMO}} - 2\sigma_{\mathrm{tot}} - \Delta\varepsilon^{\mathrm{multi-state}}_{\mathrm{UPS,onset}}. \tag{21}$$

The various correction terms on the right-hand side of this expression now refer to hole states. The shift $\Delta\varepsilon^{\mathrm{multi-state}}_{\mathrm{UPS,onset}}$ of the onset energy due to contributions from deeper-energy states is, for UPS experiments, negative, but negligibly small for the actual UPS experiments that were presented in Ref. [7].

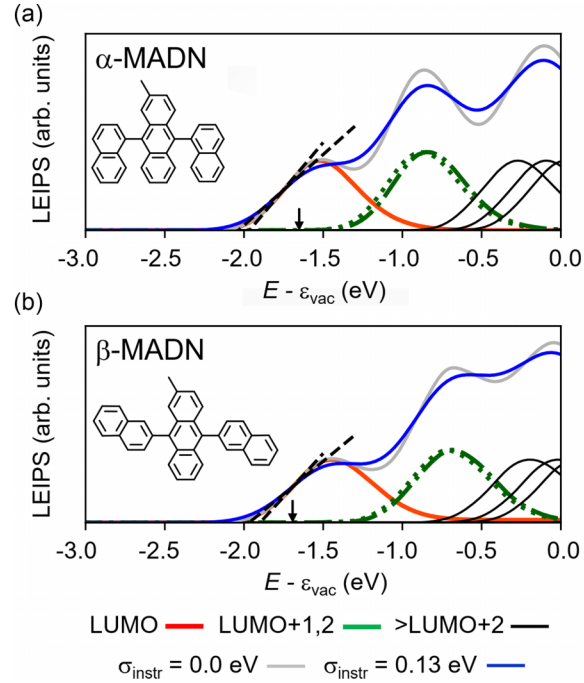


FIG. 6. Simulated LEIPS spectra for (a) α-MADN and (b) β-MADN, given as function of the difference between the final-state energy E and the vacuum level energy $\varepsilon_{\mathrm{vac}}$. Red and green curves indicate the state-dependent contributions $I_\ell(E)$ for the LUMO and the nearly degenerate LUMO+1 and LUMO+2 states, respectively. Solid black curves indicate approximated signal contributions for levels above LUMO+2 (see text). The total simulated LEIPS spectrum is, for $\sigma_{\mathrm{instr}} = 0.0$ eV, depicted by the gray curve, while the blue curve represents the spectrum with instrumental Gaussian broadening of $\sigma_{\mathrm{instr}} = 0.13$ eV. Dashed black lines indicate extrapolations from the two simulated spectra to the spectral onsets. The arrows indicate the values of the vertical bulk LUMO energies, $\varepsilon^{\mathrm{vert,bulk}}_{\mathrm{LUMO}}$. Possible effects of charging are not included.

F. Theoretical LEIPS spectra of thin films of α-MADN and β-MADN

Figure 6 shows the simulated normalized LEIPS spectra for α-MADN and β-MADN before including the instrumental broadening ($\sigma_{\mathrm{instr}} = 0.0$ eV, gray curve) and after including the instrumental broadening (blue curve) with $\sigma_{\mathrm{instr}} = 0.13$ eV (the resolution for the optical filter with the smallest full width at half maximum of its transmission curve; see Sec. IV A). The figure also shows the contributions from each separate state before including the instrumental broadening, using red (LUMO), green (LUMO+1 and LUMO+2), and black (higher-energy states) coloring. The lineshape of the LUMO peak includes contributions from vibrational broadening, energetic disorder, and the z dependence of the LUMO DOS. The spectra from the higher-energy states are approximated by shifting the *GW*/pMM SDOS by the energy difference $\varepsilon^{\mathrm{QP}}_{\ell} - \varepsilon^{\mathrm{QP}}_{\mathrm{LUMO}}$ for $\ell > 2$ from the vacuum calculation, and by using the same lineshape function as for the LUMO. Those states contribute to the spectra near the vacuum energy but,

TABLE II. Simulated vertical and adiabatic LUMO energies, LEIPS peak, and onset energies without and with instrumental broadening, and the experimental onset energies when using a 285 nm band-pass filter (all in eV), with $\sigma_{\text{instr}} \approx 0.13$ eV. The instrumental broadening σ_{instr} is defined as the standard deviation of the Gaussian instrumental resolution function. The value of 0.13 eV corresponds to a full width at half maximum of about 0.30 eV. The LUMO energies are expressed with respect to the vacuum level energy.

			Peak	Onset (σ_{instr})		
	$\varepsilon_{\text{LUMO}}^{\text{vert,bulk}}$	$\varepsilon_{\text{LUMO}}^{\text{ad,bulk}}$	LUMO	0.0 eV	0.13 eV	Exp.
α-MADN	−1.65 ±0.13	−1.83 ±0.13	−1.52	−1.97	−2.04	−1.81 ±0.10
β-MADN	−1.69 ±0.13	−1.83 ±0.14	−1.43	−1.90	−1.97	−1.73 ±0.15

due to the energy separation of the LUMO+1 and LUMO+2 peaks from the LUMO energy (0.68 eV for both MADN isomers), they do not contribute to the spectral onset energies. Possible effects of charging are not included.

Before including instrumental broadening, the calculated peak positions and onsets of the LUMO contributions to the spectra are −1.52 eV and −1.97 eV for α-MADN, and −1.43 eV and −1.90 eV for β-MADN. After including instrumental broadening, the onset energies are shifted to −2.04 eV for α-MADN and −1.97 eV for β-MADN. A peak structure is still visible. Table II gives an overview of the simulated vertical and adiabatic LUMO energies, the peak and onset energies that characterize the calculated LEIPS spectra. We note that the onset energies were found to depend only weakly on the assumed depth sensitivity of the experiment, characterized by the attenuation length Λ. When varying Λ from 2 to 8 nm, the onset energy was found to vary from −2.05 eV to −2.02 eV (α-MADN) and from −1.97 eV to −1.96 eV (β-MADN). The data that are given in Table II have been obtained for $\Lambda = 4$ nm. The last column gives the experimental onset energies, which will be discussed in Sec. IV A.

We note that for both MADN derivatives, the peak shapes are not precisely Gaussian, but exhibit a wider tail towards higher energies. This is mainly due to the asymmetry of the vibronic response function [see Fig. 5 of Ref. [7] and Fig. 5(b)]. The calculated full width at half maximum (FWHM) is about 0.5 eV for both isomers, with the β-MADN ones wider by about 0.03 eV. For a Gaussian distribution, a FWHM of 0.50 eV corresponds to $\sigma = 0.21$ eV. For α-MADN, this is close to the value of 0.19 eV that would be expected when using Eq. (18), which assumes a Gaussian distribution of all contributions to the LUMO peak width with theoretical standard deviations of $\sigma_{\text{dis}} = 0.14$ eV, $\sigma_{\text{vibr}} = 0.12$ eV, and $\sigma_{\text{surf}} = 0.05$ eV. For β-MADN, the larger LUMO disorder energy ($\sigma_{\text{dis}} = 0.19$ eV) would be expected to lead to a Gaussian width of 0.23 eV.

IV. LEIPS EXPERIMENTS

A. Method and results

LEIPS experiments of thin films of α-MADN and β-MADN were carried out using the measurement setup that was described in Ref. [76] and in references therein, using an improved photodetection method that has been described in Ref. [77]. Indium tin oxide (ITO) coated glass plates were used as a substrate. The ITO surface was first washed in acetone and isopropanol and then treated by UV/ozone cleaning. Thin films with thicknesses of 10 and 15 nm were prepared by vacuum deposition, using a deposition rate of 1 nm/min. The LEIPS measurements were performed without exposing the samples to air, at detection wavelengths of 260 and 285 nm. A Hamamatsu R821s photomultiplier was used as a photon detector. Due to a very large ratio between the quantum efficiency at the targeted detection wavelengths and at longer wavelengths in the visible range, a possible contribution to the intensity from electron-impact-induced fluorescence of the films is avoided [77]. The instrumental broadening σ_{instr} is determined by the convolution of the transmission function of the optical filter and the kinetic-energy distribution of the electrons. The kinetic-energy distribution has a Gaussian shape, with a full width at half maximum of ∼0.25 eV. Even though the transmission functions have a more rectangular shape (see Ref. [61] for the 285 filter and Ref. [77] for the 260 nm filter), the convolution has a near-Gaussian shape. For the 285 nm filter, the resolution (standard deviation of the Gaussian distribution) is $\sigma_{\text{instr}} \approx 0.13$ eV, while it is $\sigma_{\text{instr}} \approx 0.15$ eV for the 260 nm filter.

The measurement procedure involved a methodology for compensating for possible charging effects. For that purpose, measurements of the photon spectral intensity as a function of the incident electron energy, defined with respect to the Fermi energy of the metal substrate, are combined with a measurement of the work function of the system that follows from low-energy electron transmission (LEET) measurements [75]. LEET experiments probe the variation of the sample current with the energy of a monochromatic beam of incident electrons, also expressed with respect to the substrate Fermi energy. The onset energy of this current provides the work function. When the current densities that are used in both experiments are equal, such a procedure compensates for the effect of charging due to the electron beam. As was shown in Sec. III C, this compensation is only fully adequate at the vacuum interface, as charging changes the depth profile of the LUMO energies.

Figure 7 shows the LEIPS spectra for 10 and 15 nm films, obtained for both isomers at two detection wavelengths. The onset energies that are indicated in the figure are obtained by linearly extrapolating the spectral intensity in the energy range around −1 eV to the background level. For α-MADN [Fig. 7(a)], the onset energies are, on average, equal to −1.85 eV. The onset energies are, on average, 0.1 eV more negative for the spectra that have been obtained using the 260 nm filter, as compared to the results that were obtained using the 285 nm filter. Even though a downward shift of the onset energy is expected from the 0.02 eV larger instrumental broadening energy σ_{instr} when using a 260 nm filter (see above), the observed effect is larger than expected. An analysis such as presented in Sec. III E (Fig. 5) would lead to a shift of only about 0.03 eV. The difference could be due to the statistical uncertainty of the experimental onset energies. For the 15 nm films, some dependence on the detection wavelength is obtained. However, this difference is also within the

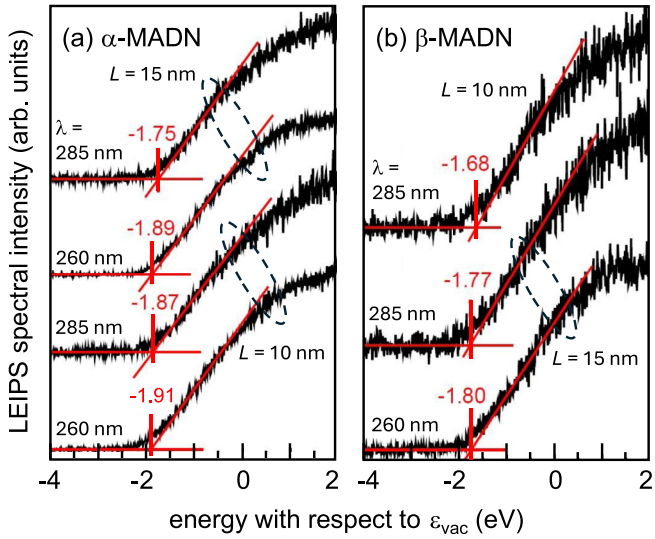


FIG. 7. LEIPS spectra obtained at two detection wavelengths ($\lambda = 260$ and 285 nm) for 10 and 15 nm films of (a) α-MADN and (b) β-MADN. The energy is expressed with respect to the vacuum level energy, ε_{vac}. The figures indicate how the spectral onset energy is determined by a linear extrapolation of the spectral intensity around an energy of -1.5 eV to the background level.

uncertainty that is expected due to the spectral noise and due to a certain ambiguity in the choice of the point from which the tangent to the background level is taken. For β-MADN [Fig. 7(b)], the average onset energy is -1.76 eV. Also in this case, the onset energy is, on average, slightly more negative for the 260 nm filter, as expected from the larger value of σ_{instr} for this filter.

B. Analysis

The onset energies that are deduced from the theoretically predicted LEIPS spectra, shown in Fig. 6, are, for both isomers of MADN, approximately 0.20–0.25 eV more negative than the experimental values that are deduced from Fig. 7. In view of the various uncertainties that are involved in the theoretical and experimental methodologies, this difference may be considered to be small. The experimental onset energies coincide, within the experimental and theoretical uncertainty margins, with the predicted adiabatic bulk values of the LUMO energy. However, we regard that as somewhat fortuitous in view of the various partially compensating effects that determine the difference between the spectral onset energy and $\varepsilon_{LUMO}^{ad,bulk}$.

A comparison between the experimental and theoretical onset energies should be made with caution because the spectra show an almost featureless increase of the intensity with increasing energy, whereas the theoretical spectra show, for both isomers of MADN, a distinct peak structure. We find that such a featureless spectral shape would be expected when the effective standard deviation of the peak intensity σ_{tot} would be about 0.35 eV, instead of the value of 0.21 eV that is expected theoretically (see Sec. III F). An additional contribution to the total distribution width of about 0.25–0.30 eV would be required to explain the observed spectral shape. We remark that we do not regard the observation of almost featureless LEIPS spectra as an indication that the lowest-energy electron states are itinerant, instead of localized. Such a situation would be expected when the transfer integrals for representative nearest-neighbor pairs would be larger than the energetic disorder energy σ_{dis} and the reorganization energy λ_{reorg}, i.e., larger than 0.1–0.2 eV. However, calculations of the transfer integrals for LUMO states on nearest-neighbor pairs with a 0.8–1.0 nm center-of-mass distance yield, for both isomers values, only $10^{-2.2\pm0.6}$ eV [24]. The uncertainty interval indicates the full width at half maximum of the distribution, when expressed on a logarithmic scale. Spectral broadening due to the formation of itinerant states is therefore not expected. We add here that analogous calculations of the transfer integrals between HOMO states yield, for both isomers, almost identical distributions as for LUMO states [24], and that the UPS spectra indeed show distinct spectral features such as expected in the case of localization [7].

A possible explanation for the discrepancy between the theoretical and experimental spectral shapes would be an additional peak broadening that is caused by charging due to the incident electron flux, either by filling intrinsic LUMO states or by filling extrinsic trap states (see Sec. III C). The direct effect is a charging-induced additional distribution width $\sigma_{ch}(d)$. However, for typical charging conditions (areal molar concentration of $c_A \sim 10^{-3}$ in the absence of traps or a volume molar concentration of $c_V \sim 10^{-3}$ in the presence of traps), σ_{ch} is expected to be only about 0.05–0.1 eV (see Sec. III C and Sec. S5 of the Supplemental Material [25]). An indirect effect of charging is a change of the LUMO energy depth profile, as shown in Fig. 3. Charging reduces the effect of the negative LUMO energy gradient of about -0.04 eV/nm in the bulk of the film and will modify the distribution width that results from the finite-depth sensitivity. For a possibly representative case, with a bulk trap density of $N_{tr} = 10^{24}$ m^{-3}, as in Fig. 3(b), and for the assumed attenuation length of $\Lambda \sim 4$ nm, the main consequence of electron trapping is expected to be a downward peak and onset energy shift of about 0.05–0.1 eV and a similar change of the distribution width. This analysis thus does not provide a possible explanation of the much larger broadening that would be required to explain the observed spectral shape. However, we cannot exclude that for the specific films studied, the actual trap densities are larger than as assumed above. For 15 nm films and $N_{tr} = 4\times10^{24}$ m^{-3}, the expected direct contribution to the distribution width is $\sigma_{ch,tr} \approx 0.26$ eV [see Sec. S5 of the Supplemental Material [25], Eq. (S12)], for which the resulting theoretical spectrum is almost featureless. We remark that the development of a LUMO energy gradient and a space charge in the film could also be influenced by illumination during or even after deposition [53] and (more indirectly) by the operation of an ion gauge pressure sensor with a hot filament that could activate residual gasses that interact with the growing film [78]. Giving an analysis of the possible resulting effects on the LEIPS spectra is beyond the scope of this work.

V. OPTICAL ABSORPTION SPECTRA AND EXCITON BINDING ENERGIES

In this section, we calculate the vertical and adiabatic singlet energies for the two isomers of MADN, and their optical

absorption spectra, and compare the calculated optical gap with the calculated charge transport gap.

A. Calculations of electron-hole excitations using the Bethe-Salpeter equation

Neutral excitations with a conserved number of electrons and with the electron and hole on the same molecule can be obtained from the Bethe-Salpeter equation (BSE) [30,79]. It determines the four-point density response function of the interacting system from the noninteracting system [31,38,80]. Coupled electron-hole amplitudes of excitation S can be expressed in a product basis of QP wave functions, i.e.,

$$\chi_S(\mathbf{r}_\mathrm{e},\mathbf{r}_\mathrm{h}) = \sum_{v}^{\mathrm{occ}}\sum_{c}^{\mathrm{unocc}} A^S_{vc}\phi_c(\mathbf{r}_\mathrm{e})\phi^*_v(\mathbf{r}_\mathrm{h}) + B^S_{vc}\phi_v(\mathbf{r}_\mathrm{e})\phi^*_c(\mathbf{r}_\mathrm{h}), \tag{22}$$

where $\mathbf{r}_\mathrm{e}$ ($\mathbf{r}_\mathrm{h}$) is for the electron (hole) coordinate. We drop the label QP for clarity. Here, A_{vc} (B_{vc}) are the expansion coefficients of the excited-state wave function in terms of resonant (antiresonant) transitions between QP occupied states v and unoccupied states c, respectively. In this basis, the BSE turns into an effective two-particle Hamiltonian problem of the form

$$\begin{pmatrix} \underline{\mathbf{H}}^{\mathrm{res}} & \underline{\mathbf{K}} \\ -\underline{\mathbf{K}} & -\underline{\mathbf{H}}^{\mathrm{res}} \end{pmatrix}\begin{pmatrix} \mathbf{A}^S \\ \mathbf{B}^S \end{pmatrix} = \Omega_S \begin{pmatrix} \mathbf{A}^S \\ \mathbf{B}^S \end{pmatrix}. \tag{23}$$

Specifically for singlet excitations, the matrix elements of the blocks $\underline{\mathbf{H}}^{\mathrm{res}}$ and $\underline{\mathbf{K}}$ are calculated as

$$H^{\mathrm{res}}_{vc,v'c'} = D_{vc,v'c'} + 2K^{\mathrm{x}}_{vc,v'c'} + K^{\mathrm{d}}_{vc,v'c'}, \tag{24}$$

$$K_{cv,v'c'} = 2K^{\mathrm{x}}_{cv,v'c'} + K^{\mathrm{d}}_{cv,v'c'}, \tag{25}$$

with

$$D_{vc,v'c'} = (\varepsilon_c - \varepsilon_v)\delta_{vv'}\delta_{cc'}, \tag{26}$$

$$K^{\mathrm{x}}_{vc,v'c'} = \int \mathrm{d}^3\mathbf{r}_\mathrm{e}\,\mathrm{d}^3\mathbf{r}_\mathrm{h}\,\phi^*_c(\mathbf{r}_\mathrm{e})\phi_v(\mathbf{r}_\mathrm{e})v_\mathrm{C}(\mathbf{r}_\mathrm{e},\mathbf{r}_\mathrm{h})\phi_{c'}(\mathbf{r}_\mathrm{h})\phi^*_{v'}(\mathbf{r}_\mathrm{h}), \tag{27}$$

$$K^{\mathrm{d}}_{vc,v'c'} = -\int \mathrm{d}^3\mathbf{r}_\mathrm{e}\,\mathrm{d}^3\mathbf{r}_\mathrm{h}\,\phi^*_c(\mathbf{r}_\mathrm{e})\phi_{c'}(\mathbf{r}_\mathrm{e}) \times W(\mathbf{r}_\mathrm{e},\mathbf{r}_\mathrm{h},\omega=0)\phi_v(\mathbf{r}_\mathrm{h})\phi^*_{v'}(\mathbf{r}_\mathrm{h}). \tag{28}$$

Here, K^{x} is the repulsive exchange interaction originating from the bare Coulomb term v_C, while the direct interaction K^{d} contains the attractive, but screened, interaction W between electron and hole, causing the binding of the electron-hole pair. In Eq. (28), it is assumed that the dynamic properties of $W(\omega)$ are negligible, and the computationally less demanding static approximation $\omega = 0$ is employed.

All GW-BSE calculations that are presented in this work have been carried out using the Gaussian-type orbital implementations in the VOTCA-XTP [32,38] software, using transitions between all 117 occupied and the lowest 117 unoccupied molecular orbitals in Eq. (22). For single molecules in the optimized geometry, the vertical excitation energies to the first excited state based on the fully analytical approach (FAA; see Sec. II A) are $\Omega^{\mathrm{FAA}}_{\mathrm{S}_1} = 3.21$ eV for both isomers. With the partial pole model (PPM; see Sec. II A) as a model frequency dependence, we obtain $\Omega^{\mathrm{PPM}}_{\mathrm{S}_1} = 3.24$ eV, so that $\Delta^{\mathrm{PPM}}_{\mathrm{FAA}} = 0.03$ eV for the S_1 state. In both cases, the excitation is formed nearly exclusively as a HOMO-LUMO transition. In the absence of additional screening due to the environment (see the strong modification of the LUMO energies from gas phase GW to polarizable GW/pMM), the vertical electron-hole binding energy $\langle S_1|2K^{\mathrm{x}} + K^{\mathrm{d}}|S_1\rangle$ is about 3.3 eV for both isomers.

Analogously to the GW/pMM embedding approach in Sec. III A for the LUMO energies, the embedded *vertical* GW-BSE/pMM S_1 energies are determined as

$$\Omega^{\mathrm{QM/MM}}_{\mathrm{S}_1,M} = \Omega^{\mathrm{intra}}_{\mathrm{S}_1,M} + \Omega^{\mathrm{inter}}_{\mathrm{S}_1,M} = \Omega^{\mathrm{intra,PPM}}_{\mathrm{S}_1,M} + \Delta^{\mathrm{PPM}}_{\mathrm{FAA}} + \Delta_{\mathrm{ZPVE}} + E^{(\mathrm{S}_1,M)}_{\mathrm{MM}} - E^{(n,M)}_{\mathrm{MM}}, \tag{29}$$

with $\Delta_{\mathrm{ZPVE}} = -0.06$ eV [81]. The contribution $E^{(\mathrm{S}_1,M)}_{\mathrm{MM}} - E^{(n,M)}_{\mathrm{MM}}$ is a pure classical energy correction due to the thin-film embedding. For the evaluation of $E^{(\mathrm{S}_1,M)}_{\mathrm{MM}}$, CHELPG partial charges are fitted to the electrostatic potential of the S_1 state and atomic polarizabilities to the excited-state polarizability $\alpha^{(\mathrm{S}_1)}_{ij} = \frac{\partial^2 E^{(\mathrm{S}_1)}}{\partial F_i \partial F_j}$, with $E^{(\mathrm{S}_1)} = E_{\mathrm{DFT}} + \Omega_{\mathrm{S}_1}$, all based on the gas phase optimal geometries. They are also used to determine the excited-state gradient $\frac{\partial E^{(\mathrm{S}_1)}}{\partial q_k}$ for the calculation of the mode-specific exciton-vibration couplings $\lambda^{\mathrm{S}_1}_k$. With that, we obtain a total exciton reorganization energy $\lambda^{\mathrm{S}_1}_{\mathrm{tot}}$ of 0.20 eV (0.21 eV) for α-MADN (β-MADN).

In the case of coupling to a single high-energy vibrational mode, with an energy $\hbar\omega_{\mathrm{vibr}} \gg k_\mathrm{B}T$, the optical absorption spectrum shows a multipeak structure ("vibronic progression") with peak distances $\hbar\omega_{\mathrm{vibr}}$. The ratios between the peak intensities are determined by the dimensionless coupling constant (Huang-Rhys factor) $\lambda^{\mathrm{S}_1}_{\mathrm{tot}}/(\hbar\omega_{\mathrm{vibr}})$ and a lowest-energy "0-0" peak at

$$E_{0-0,\mathrm{A},M} \equiv \Omega^{\mathrm{QM/MM}}_{\mathrm{S}_1,0-0,\mathrm{A},M} = \Omega^{\mathrm{QM/MM}}_{\mathrm{S}_1,M} - \lambda^{\mathrm{S}_1}_{\mathrm{tot}}. \tag{30}$$

In paper III [22] and in Fig. 9 (discussed below), it is shown that clear vibronic progressions are indeed observed in the absorption spectra for thin films of α-MADN and β-MADN, also allowing the determination of the bulk value of $E_{0-0,\mathrm{A}}$ from experiment.

In Fig. 8, we show the calculated $E_{0-0,\mathrm{A}}$ energies (blue squares), depending on the z position in the two thin films. In contrast to the behavior of the LUMO in Fig. 2, the energy of the optically active lowest exciton state does not exhibit a noticeable bending near the interfaces to the vacuum. That is due to the fact that in the classical part of the embedding, the dominant electrostatic potential change for an exciton, as compared to the ground state, stems from the dipole moment instead of the total charge. The long-range interaction with the environment and its polarization response are therefore weaker, so that the sensitivity to the environment is smaller. Similarly small effects on the energy of localized electron-hole pair excitations have been noted before, e.g., for embedded push-pull polymers [46] or small-molecule donor molecules [32]. From the calculations, we find bulk values and standard deviations of their distributions $E_{0-0,\mathrm{A}} = 3.00 \pm 0.04$ eV for α-MADN and $E_{0-0,\mathrm{A}} = 2.98 \pm 0.04$ eV for β-MADN. From the lack of a z dependence of the exciton energies, it is possible to

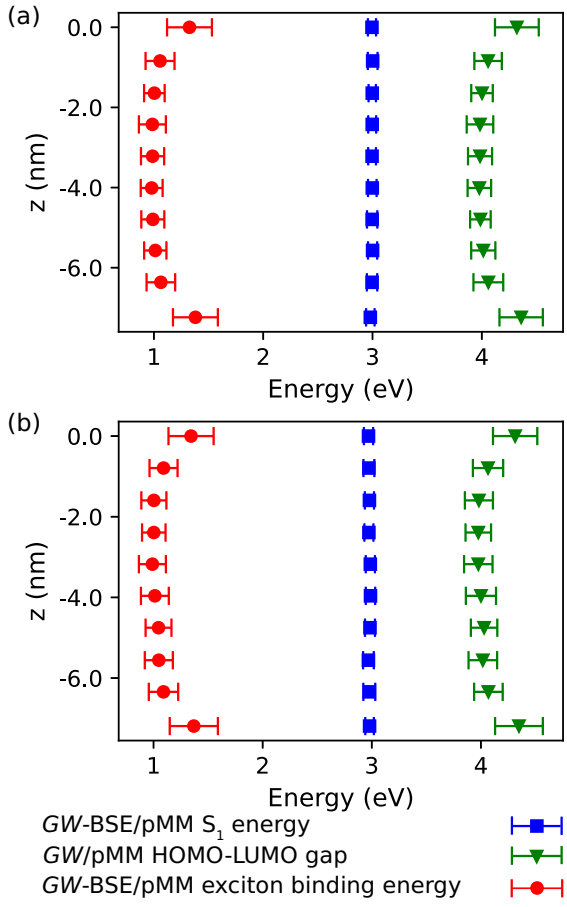


FIG. 8. Layer-resolved distributions of the difference between the ionization energy and the electron affinity (adiabatic HOMO-LUMO gaps; green triangles), the S_1 exciton energy $E_{0-0,\mathrm{A}}$ (blue squares), and the resulting exciton binding energy (red circles), obtained from polarizable *GW*-BSE/pMM calculations for thin films of (a) α-MADN and (b) β-MADN. We note that the adiabatic exciton energies are slightly smaller than the $E_{0-0,\mathrm{A}}$ values that are shown here due to the Stokes shift [see Eq. (32)], and that the adiabatic exciton binding energies [obtained using Eq. (33)] are therefore slightly larger than the values that are shown here. Table III gives the layer-averaged bulk values of all adiabatic energies.

simulate the intensity of the optical absorption spectrum as

$$I_{\mathrm{Abs}}(E) \propto \sum_M \int \delta\big[E - \Omega^{\mathrm{QM/MM}}_{\mathrm{S}_1,M}(\mathbf{r})\big] S^{\mathrm{el\text{-}vib}}_{\mathrm{S}_1,M}(\omega)\, d\omega, \qquad (31)$$

with the respective variants of Eqs. (8) and (9) with $\ell \to S_1$. The resulting spectra are shown as solid blue curves in Fig. 9 for the two isomers. Overall, the calculated spectra agree very well with the experimental reference (blue dots; spectra for solution-processed thin films shown in Fig. 5 of paper III [22]) and resolve particularly well the structure of the two lowest-energy peaks. The relative intensity of the vibrational contribution near 3.4 eV is a little too high. That may be due to excitations to higher-energy states, for which the experimental spectrum of α-MADN shows clear evidence for energies above 3.7 eV. The *GW*-BSE/pMM-based spectra result in slightly lower energies than the experimental reference. In order to facilitate comparing both spectra, we show in

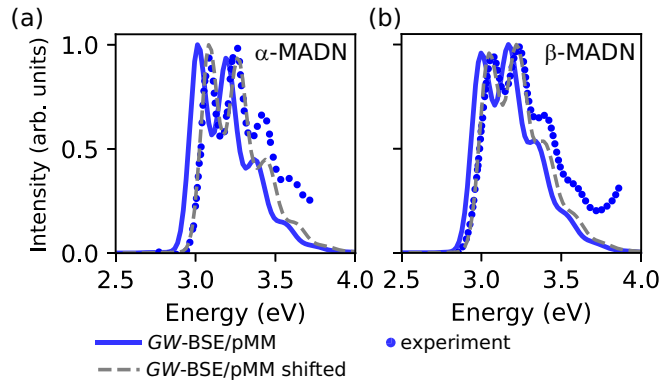


FIG. 9. Optical absorption spectra for thin films of (a) α-MADN and (b) β-MADN. Blue solid lines indicate the spectra calculated based on *GW*-BSE/pMM energies and $I_{\mathrm{Abs}}(E)$ as in Eq. (31), while the blue dots represent the experimental measurement. The dashed gray curves show the simulated spectra, shifted by 0.07 and 0.05 eV for α-MADN and β-MADN, respectively.

Fig. 9 shifted versions of the simulation results as gray dashed curves. With shifts of 0.07 and 0.05 eV for α-MADN and β-MADN, respectively, the calculated and measured spectra are practically indistinguishable up to 3.3 eV.

The average bulk $E_{0-0,\mathrm{A}}$ energies are slightly larger than the average adiabatic bulk singlet energies $\Omega^{\mathrm{ad,bulk}}_{\mathrm{S}_1}$ due to shielding of the excitations by a vibrational response of the molecules in the thin-film environment. This response is relatively slow, so that it is not probed in optical absorption experiments. It leads to a Stokes shift $\Delta E_{\mathrm{Stokes}}$ between the bulk-averaged 0-0 energies for absorption and emission, which from experiments in paper III [22] has been found to be about 0.09 and 0.17 eV for α-MADN and β-MADN, respectively. The adiabatic bulk singlet energy is given by

$$\Omega^{\mathrm{ad,bulk}}_{\mathrm{S}_1} = E_{0-0,\mathrm{A}} - \tfrac{1}{2}\Delta E_{\mathrm{Stokes}}, \qquad (32)$$

leading to $\Omega^{\mathrm{ad,bulk}}_{\mathrm{S}_1} = 2.96 \pm 0.0$ eV and 2.90 ± 0.04 eV for α-MADN and β-MADN, respectively.

B. Exciton binding energies

The layer-resolved HOMO energies from Ref. [7], the LUMO energies from Sec. III A, and the adiabatic bulk singlet exciton energies obtained above can be used to obtain the bulk value of the adiabatic singlet-exciton binding energy,

$$E^{\mathrm{ad,bulk}}_{\mathrm{bind}} = \varepsilon^{\mathrm{ad,bulk}}_{\mathrm{LUMO}} - \varepsilon^{\mathrm{ad,bulk}}_{\mathrm{HOMO}} - \Omega^{\mathrm{ad,bulk}}_{\mathrm{S}_1} \equiv E^{\mathrm{ad,bulk}}_{\mathrm{gap}} - \Omega^{\mathrm{ad,bulk}}_{\mathrm{S}_1}. \qquad (33)$$

Here, $E^{\mathrm{ad,bulk}}_{\mathrm{gap}}$ is the adiabatic charge transport (HOMO-LUMO) gap. The z dependence of the HOMO-LUMO gap is shown in Fig. 8 (green triangles). The z dependence of the individual HOMO and LUMO energies is strong, as shown in Fig. 4 of Ref. [7] and in Fig. 2. However, these gradients cancel, to a large extent, when the difference is calculated because both z dependences are caused by the same electrostatic field that results from the small net dipole moment orientation. The values of $E^{\mathrm{ad,bulk}}_{\mathrm{gap}}$ that follow from Fig. 8 are 3.98 ± 0.11 eV and 4.00 ± 0.13 eV for α-MADN and β-MADN, respectively. Near the interfaces to the vacuum, the HOMO-LUMO

TABLE III. Summary of the bulk adiabatic HOMO and LUMO energies, HOMO-LUMO gap, S_1 singlet energies, and S_1 singlet binding energies, obtained from *GW*/pMM and *GW*-BSE/pMM calculations (all in eV). The singlet binding energies have been obtained using the HOMO-LUMO gap that has been deduced directly from the z-dependent HOMO-LUMO gap energies, shown in Fig. 8. This gap (fourth entry line in the table) is slightly smaller than the gap that is obtained from the HOMO and LUMO energies that follow from analyses of their z-dependent layer-averaged values (third entry line in the table). Values in parentheses are the standard errors of their distributions.

	α-MADN	β-MADN	Reference
$\varepsilon^{\mathrm{ad,bulk}}_{\mathrm{HOMO}}$	−5.91 (0.05)	−5.89 (0.05)	Ref. [7]
$\varepsilon^{\mathrm{ad,bulk}}_{\mathrm{LUMO}}$	−1.83 (0.13)	−1.83 (0.14)	Table II
$\varepsilon^{\mathrm{ad,bulk}}_{\mathrm{LUMO}} - \varepsilon^{\mathrm{ad,bulk}}_{\mathrm{HOMO}}$	4.08 (0.11)	4.06 (0.13)	
$E^{\mathrm{ad}}_{\mathrm{gap,bulk}}$	3.98 (0.11)	4.00 (0.13)	Fig. 8
$\Omega^{\mathrm{ad,bulk}}_{\mathrm{S_1}}$	2.96 (0.04)	2.90 (0.04)	
$E^{\mathrm{ad,bulk}}_{\mathrm{bind}}$	1.02 (0.11)	1.10 (0.12)	

gap increases by about 0.3 eV due to the reduced screening of the charged excitations. With the nearly featureless z dependence of the singlet energy, the z dependence of the exciton binding energy (red spheres in Fig. 8) reflects the z dependence of the gap energy. In the bulk of the thin films, we find that $E^{\mathrm{ad,bulk}}_{\mathrm{bind}} = 1.02 \pm 0.11$ eV and 1.10 ± 0.12 eV for α-MADN and β-MADN, respectively. All bulk energies are summarized in Table III. We note that the HOMO-LUMO gap that is obtained from the bulk HOMO and LUMO energies that follow from an extrapolation of their z-dependent values, from Ref. [7] and from Table II, respectively, leads to a slightly larger gap than the direct method (from Fig. 8) that has been used above to obtain the exciton binding energies. However, the difference of ∼0.1 eV is, for both isomers of MADN, within the statistical uncertainty margin.

C. Energy-level correlations

In paper I [21], a study of field-induced dissociation in disordered organic semiconductors using kinetic Monte Carlo simulations revealed a sensitivity to correlations between the molecule-specific HOMO and LUMO energies and to correlations between the exciton energies and the HOMO-LUMO gap energies. We have studied such correlations for the two isomers of MADN. Figure 10 shows the simulation results, for molecules in the bulk of the films. The figure shows a quite strong positive correlation between the molecule-specific

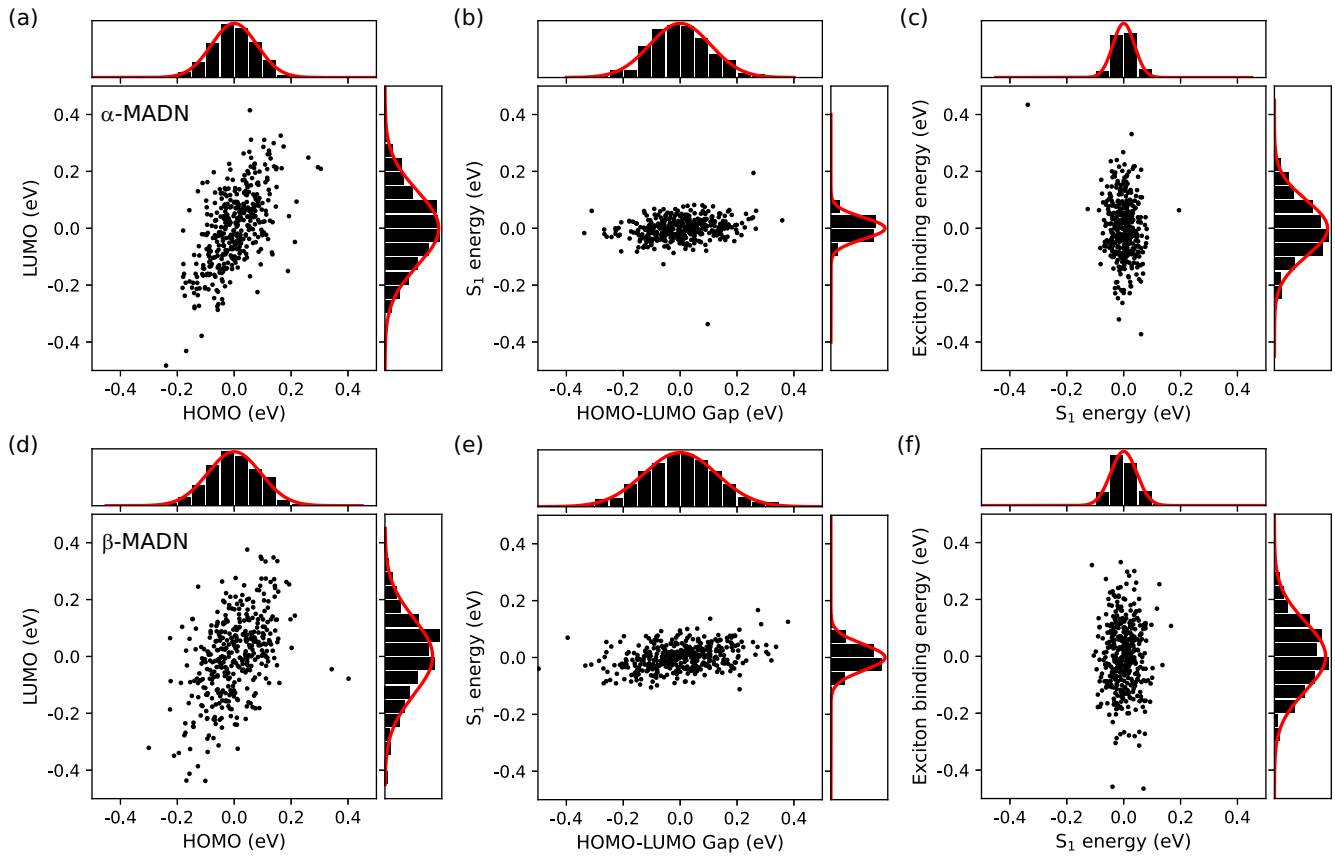


FIG. 10. Site-resolved energy-level correlations in the bulk of (a)–(c) α-MADN and (d),(e) β-MADN films. (a),(d) Correlation between the HOMO and LUMO energies. (b),(e) Correlation between the singlet S_1 energy and the HOMO-LUMO gap energy. (c),(f) Correlation between the exciton binding energy and the singlet S_1 energy. All energies are given with respect to their bulk-averaged value. The histograms show the distribution functions with a bin width of 0.05 eV. The red curves show a Gaussian approximation to the distributions. The correlation coefficients between the various distributions are given in the main text.

HOMO and LUMO and energies (correlation coefficients 0.60 and 0.47 for α and β-MADN, respectively). We note that the energies have been corrected for the gradient in the overall electrostatic field that is shown in Fig. 2. Only weak correlations are found between the molecule-specific HOMO-LUMO gaps and the singlet energies (correlation coefficients $\sim$0.21 and $\sim$0.34 for α- and β-MADN, respectively). Weak or negligible correlations are found between the singlet energies and the exciton binding energies (correlation coefficients -0.16 and 3×10^{-4} for α- and β-MADN, respectively).

VI. SUMMARY, CONCLUSIONS, AND OUTLOOK

We have presented a first-principles quantum-chemical multiscale approach for calculating the distribution of electron affinities, singlet energies, and exciton binding energies in the bulk and at the surface of thin films of disordered small-molecule organic semiconductor materials. The simulations are based on morphologies that have been obtained from a deposition simulation that uses classical force fields. Single-molecule quasiparticle energies, from which the bulk electron affinity distribution has been deduced, have been obtained in the *GW* approximation, including the effects of the electronic polarizability and static dipoles of the thin-film environment. The distribution of singlet energies has been obtained using a Bethe-Salpeter equation (BSE) approach and the distribution of exciton binding energies has been deduced by subtracting these energies from the fundamental gap that follows from the molecule-specific electron affinity that has been obtained in this work and the ionization energy that was obtained in Ref. [7]. The methodology has been demonstrated for the α and β isomers of MADN. An overview of the main numerical results has been given in Table III. This work demonstrates the feasibility of this type of simulation, with a level of accuracy and completeness that is necessary as a basis for accurate and predictive kinetic Monte Carlo simulations of the performance of optoelectronic devices such as OLEDs. The simulation results provide a support for simulation-assisted analyses of experiments that probe frontier orbital, exciton, and exciton binding energies, such as carried out in Ref. [7] and in paper III [22]. Conversely, these experiments provide a validation for the first-principles simulations. We remark that for molecules that are larger than those that have been studied in this work and that have more dihedral degrees of freedom, the accuracy of thin-film deposition simulation tools has yet to be established. However, the workflow that has been used to carry out the electronic structure and optical calculations, including the parametrization of the MM model for the electronic response, is expected to be generally applicable to disordered small-molecule-based organic semiconductors.

The validity of the predicted electron affinity has, for both isomers of MADN, been studied using LEIPS experiments. We have, for that purpose, shown how the precise spectral shape, including the peak positions and the spectral onset energy, is determined by the combined intrinsic and instrumental effects of vibronic excitations, energetic disorder, the shape of the LUMO energy profile across the film thickness and the depth sensitivity, the contributions of higher-energy peaks, and the instrumental resolution. This analysis shows that for the two isomers, a difference of about 0.15–0.20 eV may be expected between the adiabatic bulk value of the LUMO energy and the onset energy of the LEIPS spectrum. The various contributions to this difference are partially compensating, so that it is relatively small for the systems that have been studied. The analysis nevertheless shows that the onset energy as obtained from a LEIPS experiment can deviate slightly from the adiabatic LUMO energy. The onset energies that have been determined experimentally from LEIPS spectra have been found to be about 0.20–0.25 eV shallower (more positive) than the predicted value. In addition, the spectral shapes are, for both isomers of MADN, almost featureless, whereas the predicted spectral broadening is much smaller, leading to a distinct peak structure. We have developed a methodology for assessing the spectral broadening due to charging effects, including charging due to a filling of deep trap states, and have indicated under which strong trapping conditions a spectral broadening such as observed could be obtained. As an alternative explanation, we have suggested a possible effect of lateral variations of the ITO substrate work function.

The simulated optical absorption spectra have been shown to agree well with various features of the experimental absorption spectra (Fig. 9, obtained from paper III [22]), including the interpeak distance and the peak ratio in the vibronic progression. The calculated and experimental peak energies are close to 3.0 eV and differ only approximately 0.05 eV. An earlier study, in Ref. [7], already demonstrated that calculations of the ionization energy, using the same methodology as used here, are also consistent with the results of UPS experiments. However, the theoretically calculated electron affinity could not yet be validated accurately using the available LEIPS spectra, in view of the discrepancies between the theoretical and experimental spectral shapes. The finding of an experimental spectral onset energy that is about 0.20–0.25 eV higher than the theoretical value, combined with experimental optical peak energies that are about 0.05 eV larger than the theoretical values, suggests that the actual exciton binding energies could be 0.1–0.2 eV larger than the theoretically obtained values of 1.0–1.1 eV. It is therefore significant that the independent method for obtaining the exciton binding energy that has been proposed in paper I [21] and that is applied in paper III [22], using field-induced dissociation experiments, further probes the validity of the results on the electron affinity and the exciton binding energy that have been obtained in this work.

We expect that future applications of the methodology that has been presented in this paper will not only include extensions to other materials, but also various refinements of the analysis. In Sec. V C, we have studied the correlations between the HOMO and LUMO energies and between the HOMO-LUMO gap energies and the singlet exciton energies. These correlations affect the ease of field-induced dissociation, in particular for materials with relatively small exciton binding energies (see Fig. 4 of paper I [21]) such as for thermally activated delayed fluorescence (TADF) emitters. For the two isomers of MADN, the correlations between the HOMO-LUMO gap and the singlet energy or between the singlet energy and the exciton binding energy were found to be small, such as in correlation model 2, defined in Fig. 1 of paper I [21]. However, the HOMO and LUMO energies were found to show a quite strong positive correlation (correlation coefficient about 0.5–0.6), such as in correlation model 4,

defined in paper I [21]. In addition, the method is expected to enable obtaining a refined view on the effects of static molecular dipole moments on the electronic structure and the frontier orbital distribution width. Dipole moments lead to spatially correlated electronic disorder. In most charge transport studies, their effect is included by assuming a broadening of the frontier orbital energy distributions using a point-dipole approximation, leading to modified expressions for the temperature and electric field dependence of the mobility [82,83]. However, refinements beyond a point-dipole or even beyond a point-multipole approach might be needed to obtain a more proper description of the shape of the frontier orbital densities of states and of the spatial correlations between the frontier orbitals [84].

ACKNOWLEDGMENTS

We acknowledge support by the Innovational Research Incentives Scheme Vidi of the Netherlands Organisation for Scientific Research (NWO) with Project No. 723.016.002, by the NWO-project "Suppressing Exciton Quenching in OLEDs: an Integrated Approach" (SEQUOIA, Project No. 18975) of the research program "Open Technology" of the Dutch Research Council, by the Japan Society for the Promotion of Science (JSPS) Kakenhi program Grant No. 23H03939, and the Japan Science and Technology Agency (JST) Mirai program Grant No. JPMJMI20E2. Partial funding is also provided by NWO and the Netherlands eScience Center for funding through Project No. 027.017.G15, within the Joint CSER and eScience program for Energy Research (JCER 2017). We thank Vivek Sundaram for a critical reading of the manuscript.

DATA AVAILABILITY

The data that support the findings of this article are openly available [85].

[1] S. R. Forrest, *Organic Electronics: Foundations to Applications* (Oxford University Press, New York, 2020).

[2] A. Köhler and H. Bässler, *Electronic Processes in Organic Semiconductors: An Introduction* (Wiley, New York, 2015).

[3] P. Kordt, P. A. Bobbert, R. Coehoorn, F. May, C. Lennartz, and D. Andrienko, Organic light-emitting diodes, in *Handbook of Optoelectronic Device Modeling and Simulation Fundamentals, Materials, Nanostructures, LEDs, and Amplifiers*, edited by J. Piprek (CRC Press, Boca Raton, FL, 2018), Vol. 1, Chap. 15.

[4] F. Symalla, P. Friederich, S. Kaiser, T. Strunk, T. Neumann, and W. Wenzel, Computer-aided optimization of multilayer oled devices, in *SID Symposium Digest of Technical Papers* (Wiley Online Library, 2018), Vol. 49, pp. 340–342.

[5] H. Choi, G. Moon, J. Gil, J.-H. Lee, Y. Kim, J. Son, and Y. Jung, Developing novel lattice mapping for accurate and efficient charge transport modeling from atomistic morphology, J. Chem. Theory Comput. **21**, 1941 (2025).

[6] R. Coehoorn and P. A. Bobbert, Studies of OLED device performance using kinetic Monte Carlo simulations, in *Organic Electroluminescence: From Molecular Structure to Device Performance*, edited by Q. Zhang and L. Zhang (Wiley, Hoboken, New Jersey, 2025), Chap. 11, pp. 377–412.

[7] G. Tirimbò, X. de Vries, C. H. L. Weijtens, P. A. Bobbert, T. Neumann, R. Coehoorn, and B. Baumeier, Quantitative predictions of photoelectron spectra in amorphous molecular solids from multiscale quasiparticle embedding, Phys. Rev. B **101**, 035402 (2020).

[8] M.-T. Lee, C.-H. Liao, C.-H. Tsai, and C. H. Chen, Highly efficient, deep-blue doped organic light-emitting devices, Adv. Mater. **17**, 2493 (2005).

[9] C.-H. Liao, M.-T. Lee, C.-H. Tsai, and C. H. Chen, Highly efficient blue organic light-emitting devices incorporating a composite hole transport layer, Appl. Phys. Lett. **86**, 203507 (2005).

[10] M.-H. Ho, Y.-S. Wu, S.-W. Wen, M.-T. Lee, T.-M. Chen, C. H. Chen, K.-C. Kwok, S.-K. So, K.-T. Yeung, Y.-K. Cheng, and Z.-Q. Gao, Highly efficient deep blue organic electroluminescent device based on 1-methyl-9,10-di(1-naphthyl)anthracene, Appl. Phys. Lett. **89**, 252903 (2006).

[11] J. Huang, J.-H. Su, and H. Tian, The development of anthracene derivatives for organic light-emitting diodes, J. Mater. Chem. **22**, 10977 (2012).

[12] D. H. Ahn, J. H. Jeong, J. Song, J. Y. Lee, and J. H. Kwon, Highly efficient deep blue fluorescent organic light-emitting diodes boosted by thermally activated delayed fluorescence sensitization, ACS Appl. Mater. Interfaces **10**, 10246 (2018).

[13] H. Yoshida, Measuring the electron affinity of organic solids: An indispensable new tool for organic electronics, Anal. Bioanal. Chem. **406**, 2231 (2014).

[14] H. Yoshida, Principle and application of low energy inverse photoemission spectroscopy: A new method for measuring unoccupied states of organic semiconductors, J. Electron Spectrosc. Relat. Phenom. **204**, 116 (2015).

[15] H. Yoshida, Low-energy inverse photoemission study on the electron affinities of fullerene derivatives for organic photovoltaic cells, J. Phys. Chem. C **118**, 24377 (2014).

[16] H. Yoshida and K. Yoshizaki, Electron affinities of organic materials used for organic light-emitting diodes: A low-energy inverse photoemission study, Org. Electron. **20**, 24 (2015).

[17] H. Yoshida, K. Yamada, J. Tsutsumi, and N. Sato, Complete description of ionization energy and electron affinity in organic solids: Determining contributions from electronic polarization, energy band dispersion, and molecular orientation, Phys. Rev. B **92**, 075145 (2015).

[18] Y. Uemura, S. A. Abd-Rahman, S. Yanagisawa, and H. Yoshida, Quantitative analysis of the electrostatic and electronic polarization energies in molecularly mixed films of organic semiconductors, Phys. Rev. B **102**, 125302 (2020).

[19] A. Sugie, W. Han, N. Shioya, T. Hasegawa, and H. Yoshida, Structure-dependent electron affinities of perylene diimide-based acceptors, J. Phys. Chem. C **124**, 9765 (2020).

[20] A. Sugie, K. Nakano, K. Tajima, I. Osaka, and H. Yoshida, Dependence of exciton binding energy on band gap of organic semiconductors, J. Phys. Chem. Lett. **14**, 11412 (2023).

[21] E. J. de Jong, S. Gottardi, H. van Eersel, and R. Coehoorn, companion paper, Electron affinity and binding energy of excitons in disordered organic semiconductors. I. Simulation-assisted analysis of field-induced exciton dissociation experiments, Phys. Rev. B **112**, 224202 (2025).

[22] E. J. de Jong, N. G. de Rooij, W. F. M. van Geel, C. Hauenstein, H. Tomita, G. Tirimbò, M. Berghuis, S. Gottardi, B. Baumeier, and R. Coehoorn, companion paper, Electron affinity and binding energy of excitons in disordered organic semiconductors. III. Multimethod study for films of the blue fluorescent emitter MADN, Phys. Rev. B **112**, 224204 (2025).

[23] G. Tirimbó, V. Sundaram, and B. Baumeier, Embedded many-body Green's function methods for electronic excitations in complex molecular systems, WIREs Comput Mol Sci **14**, e1734 (2024).

[24] G. Tirimbò and B. Baumeier (unpublished).

[25] See Supplemental Material http://link.aps.org/supplemental/10.1103/6gh2-8lb8 for shows the calculated shapes of HOMO and LUMO orbitals, results of a study of the vibrational contribution to the relative dielectric constant, results of studies of the average escape time of absorbed electrons in LEIPS experiments, results of studies of the effect of charging by absorbed electrons on the electrostatic potential in thin films during LEIPS experiments, and results of a study of the effect of higher-energy LUMO states on the onset energy that is obtained from LEIPS experiments, which includes Refs. [27,63,74,86–89].

[26] M. Pope and C. Swenberg, *Electronic Processes in Organic Crystals and Polymers*, 2nd ed. (Oxford University Press, New York / Oxford, 1999).

[27] X. de Vries and R. Coehoorn, Vibrational mode contribution to the dielectric permittivity of disordered small-molecule organic semiconductors, Phys. Rev. Mater. **4**, 085602 (2020).

[28] A. Klamt, The COSMO and COSMO-RS solvation models, WIREs Comput. Mol. Sci. **8**, e1338 (2018).

[29] L. J. Sham and T. M. Rice, Many-Particle derivation of the effective-mass equation for the Wannier exciton, Phys. Rev. **144**, 708 (1966).

[30] L. Hedin and S. Lundqvist, Effects of electron-electron and electron-phonon interactions on the one-electron states of solids, in *Solid State Physics*, edited by F. Seitz, D. Turnbull, and H. Ehrenreich (Academic Press, New York, 1970), Vol. 23, pp. 1–181.

[31] D. Golze, M. Dvorak, and P. Rinke, The *GW* compendium: A practical guide to theoretical photoemission spectroscopy, Front. Chem. **7**, 377 (2019).

[32] G. Tirimbò, V. Sundaram, O. Çaylak, W. Scharpach, J. Sijen, C. Junghans, J. Brown, F. Z. Ruiz, N. Renaud, J. Wehner, and B. Baumeier, Excited-state electronic structure of molecules using many-body Green's functions: Quasiparticles and electron-hole excitations with VOTCA-XTP, J. Chem. Phys. **152**, 114103 (2020).

[33] W. Kohn and L. J. Sham, Self-consistent equations including exchange and correlation effects, Phys. Rev. **140**, A1133 (1965).

[34] M. S. Hybertsen and S. G. Louie, First-Principles theory of quasiparticles: Calculation of band gaps in semiconductors and insulators, Phys. Rev. Lett. **55**, 1418 (1985).

[35] W. G. Aulbur, L. Jönsson, and J. W. Wilkins, Quasiparticle calculations in solids, in *Solid State Physics*, edited by H. Ehrenreich and F. Spaepen (Academic Press, New York, 2000), Vol. 54, pp. 1–218.

[36] M. Rohlfing, Excited states of molecules from Green's function perturbation techniques, Intl. J. Quantum Chem. **80**, 807 (2000).

[37] M. Rohlfing, P. Krüger, and J. Pollmann, Efficient scheme for *GW* quasiparticle band-structure calculations with applications to bulk Si and to the Si(001)-(2x1) surface, Phys. Rev. B **52**, 1905 (1995).

[38] J. Wehner, L. Brombacher, J. Brown, C. Junghans, O. Çaylak, Y. Khalak, P. Madhikar, G. Tirimbò, and B. Baumeier, Electronic excitations in complex molecular environments: Many-body Green's functions theory in VOTCA-XTP, J. Chem. Theory Comput. **14**, 6253 (2018).

[39] F. Neese, The ORCA program system, WIREs Comput. Mol. Sci. **2**, 73 (2012).

[40] C. Adamo and V. Barone, Toward reliable density functional methods without adjustable parameters: The PBE0 model, J. Chem. Phys. **110**, 6158 (1999).

[41] R. A. Kendall, T. H. Dunning, and R. J. Harrison, Electron affinities of the first-row atoms revisited. Systematic basis sets and wave functions, J. Chem. Phys. **96**, 6796 (1992).

[42] F. Weigend, A. Köhn, and C. Hättig, Efficient use of the correlation consistent basis sets in resolution of the identity MP2 calculations, J. Chem. Phys. **116**, 3175 (2002).

[43] P. Larson, M. Dvorak, and Z. Wu, Role of the plasmon-pole model in the *GW* approximation, Phys. Rev. B **88**, 125205 (2013).

[44] N. Dupuy, S. Bouaouli, F. Mauri, S. Sorella, and M. Casula, Vertical and adiabatic excitations in anthracene from quantum Monte Carlo: Constrained energy minimization for structural and electronic excited-state properties in the JAGP ansatz, J. Chem. Phys. **142**, 214109 (2015).

[45] As in bare anthracene, the respective correction is negligible for the ionization potential (HOMO) and was not included in the results in Ref. [7].

[46] B. Baumeier, M. Rohlfing, and D. Andrienko, Electronic excitations in push-pull oligomers and their complexes with fullerene from many-body Green's functions theory with polarizable embedding, J. Chem. Theory Comput. **10**, 3104 (2014).

[47] J. Li, G. D'Avino, I. Duchemin, D. Beljonne, and X. Blase, Accurate description of charged excitations in molecular solids from embedded many-body perturbation theory, Phys. Rev. B **97**, 035108 (2018).

[48] C. M. Breneman and K. B. Wiberg, Determining atom-centered monopoles from molecular electrostatic potentials. The need for high sampling density in formamide conformational analysis, J. Comput. Chem. **11**, 361 (1990).

[49] E. G. Kratz, R. E. Duke, and G. A. Cisneros, Long-range electrostatic corrections in multipolar/polarizable QM/MM simulations, Theor. Chem. Acc. **135**, 166 (2016).

[50] A. Arnold and C. Holm, Efficient methods to compute long-range interactions for soft matter systems, in *Advanced Computer Simulation Approaches for Soft Matter Sciences II*, edited by C. Holm and K. Kremer, Advances in Polymer Science (Springer, Berlin, 2005), pp. 59–109.

[51] C. Poelking, M. Tietze, C. Elschner, S. Olthof, D. Hertel, B. Baumeier, F. Würthner, K. Meerholz, K. Leo, and D. Andrienko, Impact of mesoscale order on open-circuit voltage in organic solar cells, Nat. Mater. **14**, 434 (2015).

[52] G. D'Avino, L. Muccioli, F. Castet, C. Poelking, D. Andrienko, Z. G. Soos, J. Cornil, and D. Beljonne, Electrostatic phenomena in organic semiconductors: Fundamentals and implications for photovoltaics, J. Phys.: Condens. Matter **28**, 433002 (2016).

[53] E. Ito, Y. Washizu, N. Hayashi, H. Ishii, N. Matsuie, K. Tsuboi, Y. Ouchi, Y. Harima, K. Yamashita, and K. Seki, Spontaneous buildup of giant surface potential by vacuum deposition of Alq_3 and its removal by visible light irradiation, J. Appl. Phys. **92**, 7306 (2002).

[54] Y. Noguchi, W. Brütting, and H. Ishii, Spontaneous orientation polarization in organic light-emitting diodes, Jpn. J. Appl. Phys. **58**, SF0801 (2019).

[55] E. Tsiper, Z. Soos, W. Gao, and A. Kahn, Electronic polarization at surfaces and thin films of organic molecular crystals: PTCDA, Chem. Phys. Lett. **360**, 47 (2002).

[56] H. Yoshida and N. Sato, A precise analysis of the core-level energy difference between the surface and bulk region of organic semiconductor thin films, J. Phys. Chem. C **116**, 10033 (2012).

[57] A. Kahn, Fermi level, work function and vacuum level, Mater. Horiz. **3**, 7 (2016).

[58] R. Coehoorn, X. Lin, C. H. L. Weijtens, S. Gottardi, and H. van Eersel, Three-dimensional modeling of organic light-emitting diodes containing molecules with large electric dipole moments, Phys. Rev. Appl. **16**, 034048 (2021).

[59] X. de Vries, P. Friederich, W. Wenzel, R. Coehoorn, and P. A. Bobbert, Full quantum treatment of charge dynamics in amorphous molecular semiconductors, Phys. Rev. B **97**, 075203 (2018).

[60] T. Petrenko and F. Neese, Analysis and prediction of absorption band shapes, fluorescence band shapes, resonance Raman intensities, and excitation profiles using the time-dependent theory of electronic spectroscopy, J. Chem. Phys. **127**, 164319 (2007).

[61] H. Yoshida, Near-ultraviolet inverse photoemission spectroscopy using ultra-low energy electrons, Chem. Phys. Lett. **539–540**, 180 (2012).

[62] T. Aihara, S. A. Abd-Rahman, and H. Yoshida, Metal screening effect on energy levels at metal/organic interface: Precise determination of screening energy using photoelectron and inverse-photoelectron spectroscopies, Phys. Rev. B **104**, 085305 (2021).

[63] H. Bässler, Charge transport in disordered organic photoconductors. A Monte Carlo simulation study, Phys. Stat. Sol. B **175**, 15 (1993).

[64] S. L. M. Van Mensfoort, R. J. De Vries, V. Shabro, H. P. Loebl, R. A. J. Janssen, and R. Coehoorn, Electron transport in the organic small-molecule material BAlq—The role of correlated disorder and traps, Org. Electron. **11**, 1408 (2010).

[65] H. T. Nicolai, M. Kuik, G. A. H. Wetzelaer, B. De Boer, C. Campbell, C. Risko, J. Brédas, and P. W. M. Blom, Unification of trap-limited electron transport in semiconducting polymers, Nat. Mater. **11**, 882 (2012).

[66] M. Mesta, M. Carvelli, R. J. De Vries, H. Van Eersel, J. J. M. Van Der Holst, M. Schober, M. Furno, B. Lüssem, K. Leo, P. Loebl *et al.*, Molecular-scale simulation of electroluminescence in a multilayer white organic light-emitting diode, Nat. Mater. **12**, 652 (2013).

[67] N. B. Kotadiya, A. Mondal, P. W. M. Blom, D. Andrienko, and G.-J. A. H. Wetzelaer, A window to trap-free charge transport in organic semiconducting thin films, Nat. Mater. **18**, 1182 (2019).

[68] O. Sachnik, X. Tan, D. Dou, C. Haese, N. Kinaret, K.-H. Lin, D. Andrienko, M. Baumgarten, R. Graf, G.-J. A. H. Wetzelaer *et al.*, Elimination of charge-carrier trapping by molecular design, Nat. Mater. **22**, 1114 (2023).

[69] R. Rohloff, N. B. Kotadiya, N. I. Crăciun, P. W. M. Blom, and G. A. H. Wetzelaer, Electron and hole transport in the organic small molecule α-NPD, Appl. Phys. Lett. **110**, 073301 (2017).

[70] W. S. M. Werner, F. Simperl, F. Blödorn, J. Brunner, J. Kero, A. Bellissimo, and O. Ridzel, Energy dissipation of fast electrons in polymethylmethacrylate: Toward a universal curve for electron-beam attenuation in solids between 0 eV and relativistic energies, Phys. Rev. Lett. **132**, 186203 (2024).

[71] J. D. Bourke and C. T. Chantler, Electron energy loss spectra and overestimation of inelastic mean free paths in many-pole models, J. Phys. Chem. A **116**, 3202 (2012).

[72] M. P. Seah and W. A. Dench, Quantitative electron spectroscopy of surfaces: A standard data base for electron inelastic mean free paths in solids, Surf. Interf. Anal. **1**, 2 (1979).

[73] E. Cartier and P. Pfluger, Transport and relaxation of hot conduction electrons in an organic dielectric, Phys. Rev. B **34**, 8822 (1986).

[74] Y. Ozawa, Y. Nakayama, S. Machida, H. Kinjo, and H. Ishii, Maximum probing depth of low-energy photoelectrons in an amorphous organic semiconductor film, J. Electr. Spectr. Rel. Phen. **197**, 17 (2014).

[75] M. Kubo and H. Yoshida, Electron affinities of small-molecule organic semiconductors: Comparison among cyclic voltammetry, conventional inverse photoelectron spectroscopy, and low-energy inverse photoelectron spectroscopy, Org. Electron. **108**, 106551 (2022).

[76] H. Yoshida, Note: Low-energy inverse photoemission spectroscopy apparatus, Rev. Sci. Instrum. **85**, 016101 (2014).

[77] A. Akatsuka, M. Miura, G. Kapil, S. Hayase, and H. Yoshida, Direct measurement of electron affinity of carbazole-based self-assembled monolayer used as hole-selective layer in high-efficiency perovskite solar cells, Appl. Phys. Lett. **124**, 241603 (2024).

[78] Y. Noguchi, N. Sato, Y. Miyazaki, and H. Ishii, Light-and ion-gauge-induced space charges in tris-(8-hydroxyquinolate) aluminum-based organic light-emitting diodes, Appl. Phys. Lett. **96**, 143305 (2010).

[79] G. Strinati, Application of the Green's functions method to the study of the optical properties of semiconductors, Riv. Nuovo Cim. **11**, 1 (1988).

[80] G. Onida, L. Reining, and A. Rubio, Electronic excitations: Density-functional versus many-body Green's-function approaches, Rev. Mod. Phys. **74**, 601 (2002).

[81] The ZPVE correction for the S_1 state has been estimated using time-dependent DFT.

[82] S. V. Novikov, D. H. Dunlap, V. M. Kenkre, P. E. Parris, and A. V. Vannikov, Essential role of correlations in governing charge transport in disordered organic materials, Phys. Rev. Lett. **81**, 4472 (1998).

[83] M. Bouhassoune, S. L. M. Van Mensfoort, P. A. Bobbert, and R. Coehoorn, Carrier-density and field-dependent charge-carrier mobility in organic semiconductors with correlated Gaussian disorder, Org. Electron. **10**, 437 (2009).

[84] F. May, B. Baumeier, C. Lennartz, and D. Andrienko, Can lattice models predict the density of states of amorphous

organic semiconductors? Phys. Rev. Lett. **109**, 136401 (2012).

[85] G. Tirimbò, O. Nagaoka, S. Fukushima, C. van Hoesel, H. Yoshida, R. Coehoorn, and B. Baumeier, *Data for Paper "Electron Affinity and Binding Energy of Excitons in Disordered Organic Semiconductors. II. First-Principles Simulations and Inverse Photoemission Studies for MADN"* (4TU. ResearchData, 2025).

[86] M. Sparks, D. L. Mills, R. Warren, T. Holstein, A. A. Maradudin, L. J. Sham, E. Loh Jr, and D. F. King, Theory of electron-avalanche breakdown in solids, Phys. Rev. B **24**, 3519 (1981).

[87] D. M. Hudgins and S. A. Sandford, Infrared spectroscopy of matrix isolated polycyclic aromatic hydrocarbons. 1. PAHs containing two to four rings, J. Phys. Chem. A **102**, 329 (1998).

[88] A. Miller and E. Abrahams, Impurity conduction at low concentrations, Phys. Rev. **120**, 745 (1960).

[89] The 3D-KMC simulations have been carried out using the bumblebee simulation software tool, provided by Software for Chemistry & Materials B.V. (SCM), scm.com.